



UNIVERSITEIT VAN AMSTERDAM

**LIGHT-OUTCOUPLING MANIPULATION OF PEROVSKITE  
LEDs VIA NANO- PATTERNING OF THE ACTIVE LAYER**

*A proof of concept to pattern nanostructures into perovskite light emitting diodes*

**DAVID LANGHORST**

*stud.nr: 10534865*



MASTER THESIS: 60EC

SEPTEMBER 2020 - AUGUST 2021

MASTER OF PHYSICS AND ASTRONOMY: SCIENCE FOR ENERGY AND  
SUSTAINABILITY

1<sup>st</sup> EXAMINOR: ALBERT POLMAN | 2<sup>nd</sup> EXAMINOR: BRUNO EHRLER

SUPERVISORS: LORETA MUSCARELLA & ANDREA CORDARO

David Langhorst: *Light-outcoupling Manipulation of Perovskite Enhancing LEDs via Nano-Patterning of the Active Layer*, A master thesis that shows a proof of concept to pattern nanostructures into perovskite light emitting diodes, Master's Physics and Astronomy, Science for Energy and Sustainability ©, August 2021, Amsterdam



I have not failed, I've just found 10.000 ways that don't work.

— Thomas Edison



## ABSTRACT

---

A proof of concept is presented to manipulate light outcoupling by fabrication of nanophotonic structures in perovskite ( $\text{MAPbBr}_3$ ) light-emitting diodes (PeLED). Unpatterned full-stack devices are optimised to be reproducible in performance to be compared to the nanopatterned devices. Optimisation of the emissive  $\text{MAPbBr}_3$  led to small grains with modest roughness ( $\text{RMS} \approx 7.2\text{nm}$ ). The  $\text{MAPbBr}_3$  generates green photons with a bandgap energy of 2.3 eV, and electro- & photoluminescence showed an FWHM of  $\approx 18\text{ nm}$ . JVL measurements are carried out to calculate the PeLED current efficacy. The optimised unpatterned devices have a turn-on voltage around 3 V and a mean current efficacy of at  $15.8 \cdot 10^{-5}\text{ cd/A}$ . The pattern is fabricated by stamping a solgel layer between the HIL and the perovskite using soft conformal imprint lithography. Patterned and unpatterned devices show similar  $\text{MAPbBr}_3$  crystallisation, and green light is again generated in the patterned PeLED. The current efficacy is lower in patterned devices with a performance of  $1.6 \cdot 10^{-5}\text{ cd/A}$ . As proof of concept, this work shows the ability to fabricate a nanostructured emissive layer in PeLEDs.



## ACKNOWLEDGEMENTS

---

I would like to thank:

Foremost, my supervisor, Loreta Muscarella for great guidance and help during this project. You taught me to grow as a scientist and to grow as a person. Also, my other supervisor Andrea Cordaro, for simulating the stamp and also guiding me through this project. Bruno Ehrler for being my examiner and as group leader of the Hybrid Solar Cells group, the group where I am part of, to give me the opportunity to do my internship at AMOLF and to guide me during my internship. Albert Polman for being my examiner and for also giving me this chance to do my master's project at AMOLF. My office mates Toon Maassen, Christian Dielemans and Benjamin Daiber and Menke Knol for the great work environment. Gianluca Grimaldi for your advise and guidance and help with python. Yorick Bleiji for your experience with the AFM. The cleanroom staff and Marc Duursma for keeping the labs running and for assistance when needed. And last but not least, the Hybrid Solar Cells group in general for a great and interesting time during my internship. It was great working with you all and wish everyone the best. Onwards & upwards!





## CONTENTS

---

1	INTRODUCTION LEDS AND PELEDs	1
2	THEORETICAL BACKGROUND	5
2.1	Conventional Light Emitting Diode . . . . .	5
2.2	Perovskite & PeLEDs . . . . .	8
2.2.1	Perovskites . . . . .	8
2.2.2	Perovskite LEDs . . . . .	9
2.2.3	Geometry LED Measurement and Characteriza- tion . . . . .	11
2.3	Total internal reflection problem and outcoupling en- hancement via nanopatterns . . . . .	17
2.4	Soft Comformal Imprint Lithography (SCIL) . . . . .	19
3	METHOD SECTION	21
3.1	Fabrication PeLEDs . . . . .	21
3.1.1	Substrate and Cleaning . . . . .	21
3.1.2	Precursor Fabrication & Other Materials . . . . .	22
3.1.3	Spincoat Processes . . . . .	22
3.1.4	Thermal Evaporator . . . . .	24
3.2	Characterization measurements . . . . .	25
3.2.1	JVL measurements . . . . .	25
3.2.2	Thickness, roughness and surface morphology . . . . .	25
3.2.3	XRD, UV-Vis and PL . . . . .	26
3.2.4	Measurements for Simulation . . . . .	27
4	RESULTS EN DISCUSSION	29
4.1	Flat Devices . . . . .	29
4.2	Patterned Devices . . . . .	33
4.3	Discussion . . . . .	38
5	CONCLUSION AND OUTLOOK	43
5.1	Conclusion . . . . .	43
5.2	Outlook . . . . .	44
A	APPENDIX	45
	BIBLIOGRAPHY	51

## LIST OF FIGURES

Figure 1	Fraction of power outcoupled versus losses after radiative recombination; a significant fraction of power is lost as waveguide modes and a smaller fraction is outcoupled emission <sup>[8]</sup> . . . . .	2
Figure 2	a) Schematic drawing of LED under forward bias; b) the energy band diagram under forward bias condition showing light after recombination source: [11] . . . . .	6
Figure 3	Schematic overview of perovskite crystal where A is a monovalent organic or inorganic cation, B is a divalent metallic cation and X are halide anions <sup>[15]</sup> . . . . .	8
Figure 4	Device structure flat device with a bottom-up fabrication. . . . .	10
Figure 5	Band alignment PeLED with values given respectively to the workfunction in eV. . . . .	11
Figure 6	Characterization geometry setup . . . . .	12
Figure 7	Responsivity photodetector OSD50-E <sup>[24]</sup> . . . . .	13
Figure 8	Normalised electroluminescence LED . . . . .	14
Figure 9	Photopic factor from the human eye as function of wavelength. Here is shown that the optimum is around 555 nm which is in the green regime (515-570 nm) <sup>[22]</sup> . . . . .	15
Figure 10	CIE colour scheme with PL spectra from perovskites versus NTSC colour standard and conventional LED TV colours. The black lines indicate the perovskite colour gamut <sup>[4]</sup> . . . . .	16
Figure 11	Waveguiding from conventional optical perspective . . . . .	17
Figure 12	Absorption spectra and photoluminescence . . . . .	18
Figure 13	On the left a metasurface with emitters is for simulation calculation the same as incident external light that excites the near field in the metasurface <sup>[30]</sup> . . . . .	19
Figure 14	Schematic of a SCIL stamp where the thin glass holds the two-layer silicone rubber stamps. The high-modulus PDMS layer (red) is X-PDMS and contains the patterns. The low modulus (light green), helps to make better contact with the surface. <sup>[31]</sup> . . . . .	20

Figure 15	1) Solgel spincoated on top of ITO/PEDOT:PSS. 2) The SCIL stamp is directly placed on top of the solgel. 3) The solgel needs to cure for 6 minutes in order to make proper patterns. 4) After 6 minutes the stamp can be removed smoothly and the solgel will be left with nanostructures. <i>This illustration is based on the Verschuur article<sup>[31]</sup> and adjusted to this work's application.</i> . . . . .	20
Figure 16	Real and schematic view from a perovskite LED substrate. . . . .	21
Figure 17	Absorption spectra and photoluminescence . .	29
Figure 18	PL versus EL . . . . .	30
Figure 19	X-ray diffraction flat device with on the x-axis the degrees and on the y-axis the normalized counts. . . . .	31
Figure 20	Scanning Electron Microscopy from MAPbBr <sub>3</sub> spincoated on top of ITO and PEDOT:PSS. Crystallization dimensions are relatively small (<200 nm) . . . . .	31
Figure 21	Atomic Force Microscopy of MAPbBr <sub>3</sub> spincoated and annealed on top of PEDOT:PSS. The dimensions of this AFM measurement is 10 x 10 $\mu$ m in order to give an overview of the homogeneity of the emissive layer. . . . .	32
Figure 22	(a) Shows PeLED under operation at $\pm 7.0$ V; (b) Shows example measurement of pixel during voltage sweep. . . . .	33
Figure 23	Current efficacy presented as a distribution of performance of flat devices. . . . .	33
Figure 24	Simulated results for flat and patterned device plotted together with the by the EL spectra . .	34
Figure 25	Simulated pattern dimensions . . . . .	35
Figure 26	Unetched solgel on top of PEDOT:PSS and ITO	35
Figure 27	The glass substrate at the bottom stacked with ITO layer ( $\pm 100$ nm), PEDOT:PSS layer ( $\pm 40$ -50 nm) and the solgel nanopatterns on top. . . . .	36
Figure 28	XRD patterned device crystallized on top of ITO and PEDOT:PSS . . . . .	36
Figure 29	The glass substrate at the bottom stacked with ITO layer ( $\pm 100$ nm), PEDOT:PSS layer ( $\pm 40$ -50 nm) and the solgel nanopatterns on top . . . . .	37
Figure 30	SEM of heated precursor solution before spincoat procedure. . . . .	37

Figure 31	Distribution of patterned devices with on the x-axis the current efficacy and on the y-axis the probability of finding that efficacy. . . . .	38
Figure 32	H-field enhancement . . . . .	45
Figure 33	E-field enhancement . . . . .	46
Figure 34	Fitted data from ellipsometry data from MAPbBr <sub>3</sub> and PEDOT:PSS where n is the refractive index and k the extinction coefficient . . . . .	47
Figure 35	AFM PEDOT:PSS layer on top of ITO/glass substrate. . . . .	48
Figure 36	(001) Peak showed almost complete overlap in XRD measurements. . . . .	48
Figure 37	This figure shows the raw data from the watershed measurements. The y-axis show the counts and the x-axis the grain size radius . . . . .	49

## LIST OF TABLES

---

Table 1	Energy band gap, emitting wavelength, and color for some LED materials . . . . .	5
---------	---	---

## ACRONYMS

---

AFM	Atomic Force Microscopy
EL	Electroluminescence
EIL	Electron Injection Layer
EQE	External Quantum Efficiency
HIL	Hole Injection Layer
ITO	Indium Tin Oxide
JVL	Current Voltage Luminance
LED	Light-Emitting Diode
MAPbBr <sub>3</sub>	Methylammonium lead bromide
OIHP	Organic Inorganic Halide Perovskite
OLED	Organic Light-Emitting diode
PeLED	Perovskite Light-Emitting Diode
PL	Photoluminescence
PLQY	Photoluminescent Quantum Yield
PSC	Perovskite Solar Cell
SCIL	Soft Conformal Imprint Lithography
SEM	Scanning Electron Microscopy
SSL	Solid-State Lighting
TIR	Total Internal Reflection
XRD	X-ray Diffraction

## INTRODUCTION LEDS AND PELEDs

---

Climate change is one of the biggest challenges of our times<sup>[1]</sup>. Drought, floods, wildfires and cyclones seem to be the new normal and the last decade was the hottest in human history<sup>[2]</sup>. One of the causes of the climate problem is our eternal increase in energy consumption, among which is our electricity consumption. Electrical light sources are responsible for energy consumption of around  $1/5 - 1/6$  of the worldwide electricity production<sup>[3],[4]</sup>. Therefore, it is essential to use this electrical lightning energy most efficiently. In this thesis, a proof of concept is made on manipulating a photonic device, which can theoretically increase light outcoupling. This increased outcoupling can then theoretically lead to a more efficient device.

*Why LEDs?*

Photonic devices play an essential role in society in a diverse and wide variety of applications<sup>[5]</sup>. A variety of these photonic devices, such as light-emitting diodes (LEDs), have used semiconductor materials to develop into commercial products such as LED displays in TVs and telephones. LEDs are nowadays ten times more efficient than conventional lighting in terms of energy usage<sup>[4]</sup>. The LED market is already significant, and so is its consumption. However, this display market is expected to grow even more with an annual rate of 13.2 per cent from 2020 to 2027<sup>[6]</sup>.

LEDs are solid-state lighting (SSL) devices that emit light when a current flows through the device. Due to the semiconductor material inside the diode, electrons and holes can radiatively recombine and release their energy as photons<sup>[5]</sup>. In recent years, a relatively new class of materials has appeared in semiconductor physics, including LED applications. The organic-inorganic halide perovskites (OIHP) emerged as a new family of materials suitable for LEDs<sup>[7]</sup>. Their structural formula is  $ABX_3$ , where the monovalent A-cation can be organic (such as MA or FA) or inorganic (such as  $Cs^+$ ). The metallic B-cation is metallic (such as  $Pb^{2+}$  or  $Sn^{2+}$ ) and the X are halide anions ( $Cl^-$ ,  $Br^-$  or  $I^-$ ). The advantages of the OIHPs, compared to conventional LEDs, are great optoelectronic properties for light applications. Due to the broadly tunable bandgaps, high colour purity, low cost, and solution-based fabrication, these organic-inorganic halide perovskite semiconductors possess the potential to develop into a new generation of LED technology. However, in both thin films and bulk semiconductor materials, one of the biggest problems is losses due to waveguiding inside the slab of the material, and only 20 to 25 per cent gets

*What is the problem?*



coupled out of the material<sup>[8],[9]</sup>. This is schematically drawn by Zhao et al.<sup>[8]</sup> in fig. 1.

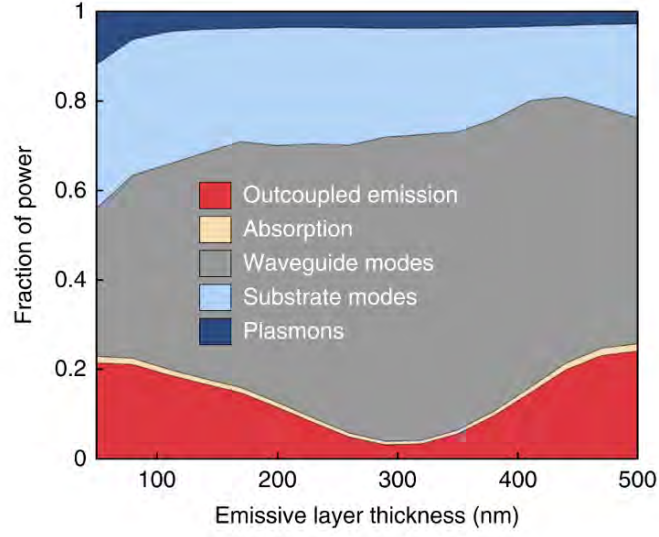


Figure 1: Fraction of power outcoupled versus losses after radiative recombination; a significant fraction of power is lost as waveguide modes and a smaller fraction is outcoupled emission<sup>[8]</sup>

Therefore, in this thesis, a study on light management in perovskite light-emitting diodes (PeLEDs) will be carried out to manipulate the active layer with nanopatterns. A proof of concept is presented on how to pattern perovskite nanostructures. As a result of these structures, a higher amount of generated light could be outcoupled outside the device which leads to a more efficient device. Optimization of the layers and interfaces between the active layer and the hole- and electron-injection material have to be performed to improve stability and enhance performances before commercialization is feasible.

At first, in this thesis, literature research will be carried out to identify the origins of the performance losses. Second, the hole injection layer and the emissive layer of the LED devices will be characterized in order to fabricate a stable and reproducible device that can be used as a reference PeLED. Atomic Force Microscopy (AFM) and Electron Scanning Microscopy (SEM) will be used to quantify the material's thickness, roughness, and surface morphology. X-ray diffraction (XRD), photoluminescence (PL), electroluminescence (EL), and UV-vis spectroscopy measurements will be used to characterize the structural and optical properties of the perovskite material. Afterwards, full characterization measurements are carried out. This characterization is an J-V-L measurement to quantify the PeLED's efficiency.

In the second part of this thesis, the flat active layer from the upper described PeLED device would be modified with a nanopatterned interlayer of solgel using Soft Conformal Imprinting Lithography<sup>[10]</sup>. This lithography method can create nanopatterns on substrate scale to enhance the light outcoupling of the perovskite active layer. The reference PeLED dimensions are used to design a theoretically optimized structure to outcouple waveguides more efficiently in the outward direction perpendicular to the active layer. Finally, the reference PeLED devices (without nanostructures) will be compared, based on performance, to the patterned PeLED devices. The results will be discussed, and a conclusion and outlook will be given.



## THEORETICAL BACKGROUND

This chapter will give a general overview of the device physics behind conventional LEDs, PeLEDs, the injection and recombination mechanisms, and the electrical and optical characteristics. The chapter starts with conventional LEDs and then elaborate extensively on the PeLEDs and their mechanisms and characterizations. At last, a description will be given of how to theoretically enhance thin-film PeLED devices by patterning the active layer with nanoscale structures to increase light outcoupling.

### 2.1 CONVENTIONAL LIGHT EMITTING DIODE

LEDs are semiconductor material light-emitting diodes that have a p-n junction. When a forward bias is applied, electrons and holes start to recombine inside the LED. An LED can emit spontaneous optical radiation if the recombination is radiative. This radiative recombination generates photons (light). The spectral emission of this emitted light can vary from the ultraviolet (UV) up to deep into the infrared (IR) [5]. This variety of differences in wavelength depends on the semiconductor material's bandgap used as active layer (emitting material). In table 1 LED semiconductor materials and their bandgap energies and corresponding wavelength are shown. As said earlier, light emission occurs when a forward bias above a certain threshold is applied across a p-n junction. This p-n junction is formed when an n-type (negatively charged) material is combined with a p-type (positively charged) material. When these materials exist in the same crystal, a semiconductor p-n junction is created.

After an applied forward bias, minority injection and radiative recombination will occur in the diodes (quasineutral regions). Radiative recombination is the phenomenon when an electron, which can

MATERIAL	ENERGY[EV]/WAVELENGTH[NM]	COLOR
InGaN	2.48-2.76 / 450 - 500	Blue
GaInP	2.18 - 2.48/ 500 - 570	Green
GaAs	<1.90/ >760	IR

Table 1: Energy band gap, emitting wavelength, and color for some LED materials<sup>[5]</sup>.

move freely in the conduction band, recombines with a hole, which is a vacancy of an electron in the valence band. The energy transition from the conduction band to the valence band escapes as excess energy in the form of a photon (light). This process is schematically drawn in Fig. 2b. Under forward bias, the electrons are injected from the n-region (right side of Fig. 2a), and the holes are injected from the p-region [11].

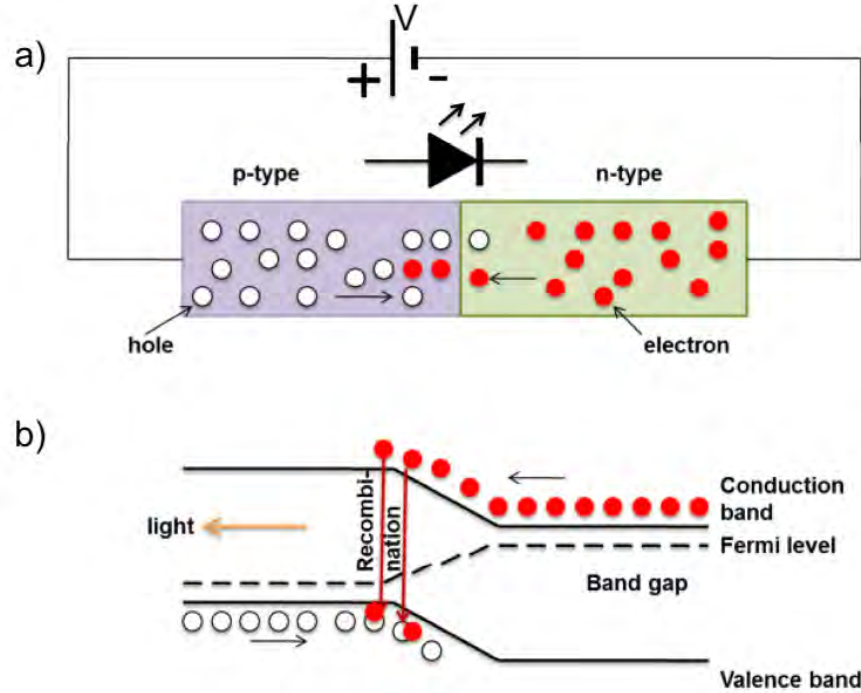


Figure 2: a) Schematic drawing of LED under forward bias; b) the energy band diagram under forward bias condition showing light after recombination source: [11]

As already mentioned, energy consumption has increased fast. lighting is an important part of this energy consumption. An approximation is made in 2018 on this fraction and shows that about 6% of all global electricity is used on lightning of homes. Additionally another 10% is used on lightning the commercial section<sup>[4]</sup>. This shows how much light is simply misused/wasted/washed due to the use of low efficiency lightning. LEDs on the other hand are considered to be around 10 times more efficient than traditional lightning from incandescent wires<sup>[4]</sup>.

However, making light from the bulk of a semiconductor p-n junction in conventional LEDs presents problems. Conventional LEDs have a lack of excitons at room temperature, fabrication has to be carried out under vacuum, tuneability is still not as straightforward, and fabrication costs after decades of fabrication are still relatively high <sup>[4]</sup> <sup>[12]</sup>.

The material costs of the emissive and transport layers are between 1.70 \$/g and 57.20 \$/g. Fabrication costs for OLEDs are even higher with only an emissive layer that can cost up to 4678 \$/g and transport layers up to 400 \$/gram <sup>[4]</sup>.

## 2.2 PEROVSKITE & PELEDs

### 2.2.1 Perovskites

A relatively new class of semiconductor materials are organic-inorganic halide perovskites (OIHPs). A schematic figure of an OIHP is shown in Fig 3. This crystal has a structural formula is  $ABX_3$  as already mentioned in the introduction. In this work methylammonium is the A-cation, the B-cation is lead and the halide is the bromide. This composition is chosen due to it's relatively simple fabrication procedure and relatively high stability compared to other OIHPs.

Although perovskites are known for almost two centuries and intensively investigated for magnetic, optical and electric properties and applications in the late 20th century, the interest in OIHPs has blown up exponential over the last decade. This interest is based on an assembly of properties that makes OIHPs highly useful as semiconductor material. OIHPs have electronic properties that show direct tunable bandgaps, proper absorption of light, balanced electron/hole effective masses, good charge mobility, and are high defect tolerance<sup>[13],[8],[9]</sup>. In addition, OIHPs have unprecedented flexibility to tune structural, optical, and electronic properties using both inorganic and organic components of OIHPs, pointing to outstanding promise for "organic-inorganic" electronics applications (source introductory to perovskite<sup>[14]</sup>). At last, their readily accessible synthesis of high-quality crystals and films enables facile structure-property correlation and rapid device optimization<sup>[13]</sup>.

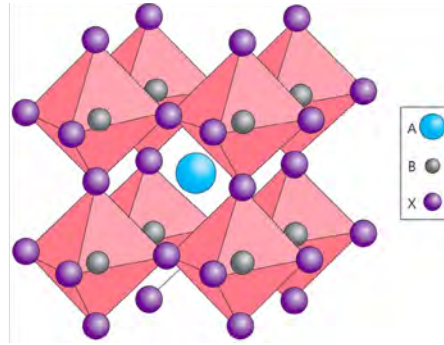


Figure 3: Schematic overview of perovskite crystal where A is a monovalent organic or inorganic cation, B is a divalent metallic cation and X are halide anions<sup>[15]</sup>

### 2.2.2 Perovskite LEDs

The reemergence of halide perovskites, now as semiconductor materials, have given rise to novel methods of producing electrical power in photovoltaic applications with the first perovskite solar cell since Miyasaka et al. reported it in 2009<sup>[16]</sup>. A rapid development prompted a couple of years later in the first PeLEDs reported in 2014 that could operate at room temperature with a 3D perovskite emissive layer<sup>[17]</sup>. A tremendous amount of research has been going on since. The external quantum efficiencies have risen from below 1% up to 22% in CsPbBr<sub>3</sub> nanocrystals<sup>[7]</sup>. However, the device performance still falls behind those of the best organic LEDs (OLEDs), which are already commercial in display technology<sup>[8]</sup>. The application requirement is >10000 hours and for green and blue PeLEDs this lifetime is hundreds of hours and several minutes respectively<sup>[4]</sup>.

The PeLED framework stems from the advancements made in OLED technologies. The injection layer materials such as PEDOT:PSS (Poly(3,4-ethylene dioxythiophene)-poly(styrene sulfonate)) and TBPi (2,2,2-(1,3,5-benzinetriyl)-tris(1-phenyl-1-H-benzimidazole)) are widely investigated for OLED applications. Furthermore, PeLED also benefits from former work in thin-film LED technologies with high optical quality films by solution-based processes and thermal evaporation techniques<sup>[7]</sup>. High-quality perovskites are essential for enhancing efficiencies and suppressing nonradiative recombination. However, creating these top notch perovskite films is a delicate work. Cho et al. showed that during nominal stoichiometry precursor fabrication, metallic lead was present<sup>[12]</sup>. This caused unintended loss of Br atoms or incomplete chemical reactions between during precursor formation. Dulkeith and colleagues showed that this metallic Pb degrade luminescence by increasing the nonradiative decay rate and decreasing the radiative decay rate<sup>[18]</sup>. By subtle changes in stoichiometric ratio in MABr:PbBr<sub>2</sub> from nominal (1:1) to (1.05:1.00), more than 10-fold PLQE enhancement is measured<sup>[12]</sup>.

In the PeLED's emissive layer, OIHP grains need to be small in order to have high quality grains. Small and high quality grains in MAPbBr<sub>3</sub> lead to a better charge distribution and the effective exciton quenching in smaller grains. This exciton quenching lead to more favourable discrete energy bands<sup>[12]</sup>. Large grainsize cuboids lead to leakage of current and a large diffusion length which causes a reduction in current efficacy<sup>[12]</sup>. To improve current efficiency, grain sizes must be decreased, and the MAPbBr<sub>3</sub> films should be flat and homogeneous without pinholes. In addition, the smaller grains can limit exciton and/or charge carrier diffusion length spatially and by doing



so, reducing possible exciton dissociation into carriers<sup>[12]</sup>.

Figure 4 shows a schematic overview of the PeLED device used in this work. The PeLED's component structure consists of a glass substrate covered with a layer of indium tin oxide (ITO). ITO is a transparent conducting material that can be used as electrode material. On top of the ITO, there is the hole injection layer. The injection layer used is PEDOT:PSS. It is a polymer mix of two charged monomers. The PEDOT is the positively charged, and the PSS is the negatively charged ionomer and collectively makes a molecular salt<sup>[19]</sup>.

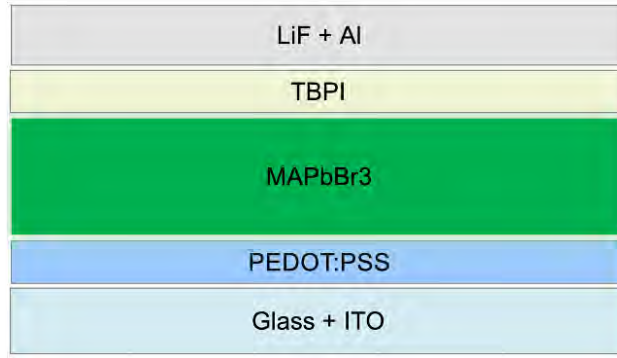


Figure 4: Device structure flat device with a bottom-up fabrication.

The next layer is the emissive layer. It is a perovskite thin film made from methylammonium lead bromide. On top of the emissive perovskite layer, the electron injection layer, called TBPI, is thermally evaporated. TBPI is a relatively large molecule compared to PEDOT:PSS and is being electron deficient. This leads to conductive properties for electrons and is therefore used as an electron transport layer material in optoelectronic devices<sup>[20]</sup>. The hole and electron injection layers do not only inject holes and electrons but also function as blocking barriers for opposite charges. So the hole and electron injection layers prevent electrons and holes to escape in unintentional directions, respectively. Additionally to the evaporation of TBPI, lithium fluoride (LiF) is evaporated on top of the TBPI layer. LiF plays a crucial role as an interlayer between the electron transport layer and the cathode material in PeLEDs. Lithium ions migrate to the cathode part and fluoride ions to the anode part. By doing so, lowering the Schottky barrier height and reducing the barrier which give higher EQE and lower turn-on voltages<sup>[21]</sup>. At last, on top of the LiF there is an aluminium cathode back contact.

As reported earlier in section 2.1 and shown in figure 2 for conventional LEDs, a forward bias is applied to inject electrons and holes into the PeLEDs. To be more specific, The electrons and holes are injected at the contacts due to this forward bias and recombine in the

crystals of the emissive MAPbBr<sub>3</sub>. The structure is designed in a way that it is energetically favourable for the electrons and holes to recombine radiatively in the perovskite emissive layer. This mechanism should, just as conventional leds, give rise to electroluminescence<sup>[7]</sup>. The band alignment of the PeLEDs used in this work are shown in figure 5.

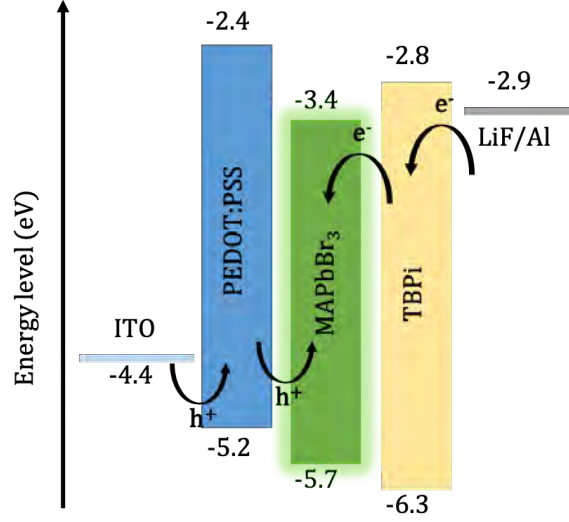


Figure 5: Band alignment PeLED with values given respectively to the work-function in eV.

### 2.2.3 Geometry LED Measurement and Characterization

In this subsection the theoretical derivation of the equations is given how later data is analysed. The approach used in this thesis to characterize the PeLEDs is to collect the photons emitted in the forward hemisphere by a large photodetector at close proximity. Both, the approach and calculations are based on work from Anaya et al. in 2019<sup>[22]</sup>. In this measurement, the distance and geometry must assure a good compromise between the detection of light, the solid angle and reduction of defects such as reflection losses and edge effects in the photodetector<sup>[22]</sup>. Therefore, it is important to take the geometrical setup into consideration. The geometry of detection determines the effective solid angle  $\Omega_{\text{phd}}$  that reaches the photodetector. Figure 6 shows the dimensions from the setup used in the thesis. The solid angle can be calculated when the dimensions of the setup are known (formulas 1 and 2)<sup>[22]</sup>. This assumption is based on the principle that the photodetector area is significantly larger than the LED pixel area  $A_{\text{phd}} \gg A_{\text{LED}}$ <sup>[23]</sup>.

$$\Omega_{\text{phd}} = 2\pi \left( 1 - \cos \frac{r_{\text{phd}}}{D} \right) \quad (1)$$

$$r_{phd} = \sqrt{\frac{A_{phd}}{\pi}} \quad (2)$$

Where  $D$  is the distance between the glass and the photodetector and  $r_{phd}$  is the radius of the photodetector.

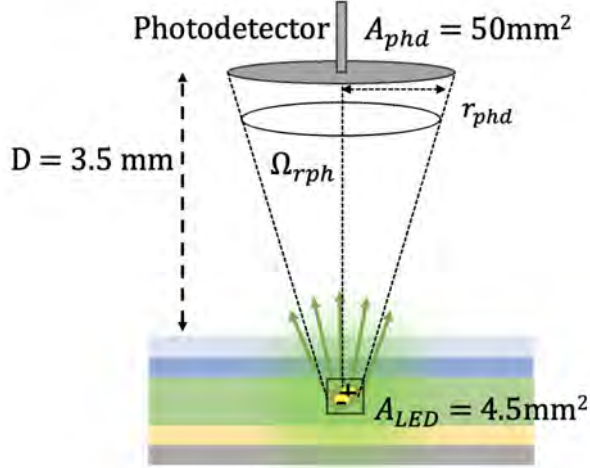


Figure 6: Characterization geometry setup

A common way to test PeLEDs is to carry out current - voltage - luminance measurements (JVL measurements). A forward bias in the form of a voltage sweep is applied during these JVL measurements. The voltage ( $V_{LED}$ ) and the current ( $I_{LED}$ ) through the LED pixels are monitored at the same time. Also during the voltage sweep, a part ( $\Omega_{phd}$ ) of the radiative recombination of electrons and holes create photons and are detected by the photodetector. The detected photons at the photodetector induce a certain current ( $I_{phd}$ ) what can be transformed to the emissivity of the LED under operating conditions which is the radiance  $\left[\frac{W}{sr \cdot m^2}\right]$ . This  $I_{phd}$  is also monitored as function of the  $V_{LED}$  during the voltage sweep. The radiance corresponds to the power from the emitted photons per unit area per solid angle which is the first step in calculating the LED efficiencies<sup>[22]</sup>.

The photodetector itself has a responsivity factor  $Q(\lambda)$  with units:  $\left[\frac{A}{W}\right]$ . This is basically how responsive the detector is for specific wavelengths. The factor itself is the conversion factor that converts the amount of generated power per ampere put in the system. This responsivity factor  $Q$  has to be weighted by the EL spectrum (Figure 8) of LED to calculate the quantum efficiency that converts the photon to electron efficiency. Weighing the responsivity factor  $Q$  with the

EL is because the distribution of generated light at a specific wavelength has to be taken into account. This value is called  $C$ . Where  $C$  is given by the following equation 3<sup>[22]</sup>. Now one is able to calculate the radiance as function of the voltage and is shown in equation 4.

$$C = \frac{\int Q(\lambda) \cdot S(\lambda) d\lambda}{\int S(\lambda) d\lambda} \quad (3)$$

$$R = \frac{I_{LED}}{C \cdot \Omega_{phd} \cdot A_{LED}} \quad (4)$$

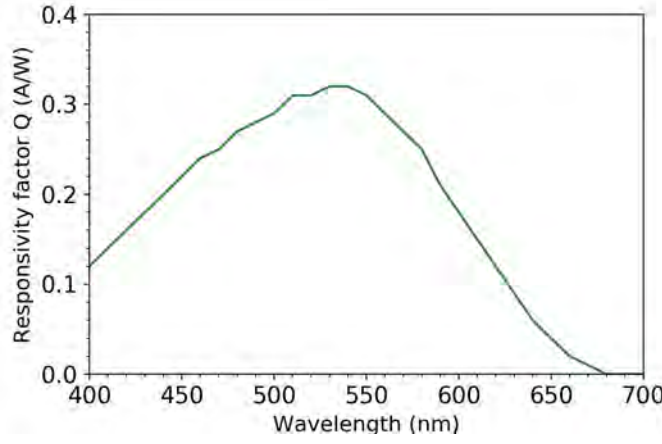


Figure 7: Responsivity photodetector OSD50-E<sup>[24]</sup>

To be able to calculate what is the amount of photons per meter squared at a specific wavelength, the electroluminescence spectrum  $S(\lambda)$  from the LED device has to be measured<sup>[22]</sup>. The EL spectrum is measured with spectrometer coupled to an optical fiber and the background has been subtracted for correction (see fig 8).

The radiance  $R$  in equation 4 divided by the area of the pixel ( $A_{LED}$ ) gives the radiant intensity  $R'$  in  $\left[\frac{W}{sr}\right]$  which enables a conversion from radiance to photon flux  $\phi_{phd}$  (5)<sup>[22]</sup>. With this photon flux, efficiency calculations can be carried out because now the amount of generated photons from the PeLED is known.

$$\phi_{phd} = \frac{R'}{E_{photon}} \quad (5)$$

Where the photon energy  $E_{photon}$  is the average energy per photon emitted from the LED. This can be calculated by multiplying the normalised EL spectrum by its corresponding photon energy and weigh

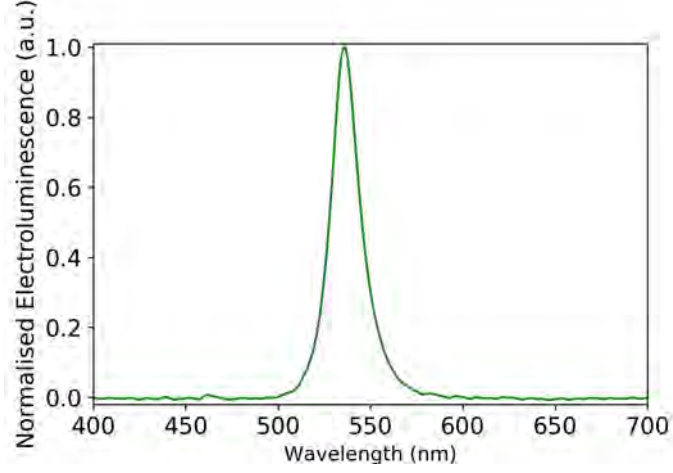


Figure 8: Normalised electroluminescence LED

this by the normalised EL spectrum  $S(\lambda)$  to get the weighted photon energy average. This is also shown in equation 6 [22].

$$E_{\text{photon}} = \frac{\int S(\lambda) \cdot \frac{hc}{\lambda} d\lambda}{\int S(\lambda) d\lambda} \quad (6)$$

Since the  $\phi_{\text{phd}}$  is only a part of the total generated light in the forward hemisphere, the resulting photon flux  $\Phi$  can be calculated in the entire forward hemisphere. This is true under the assumption that the LED emission is an Lambertian emitter [22]. Then the resulting photon flux  $\Phi$  is eventually the  $\phi_{\text{phd}}$  multiplied with  $\pi$ .

$$\Phi = \frac{1}{E_{\text{photon}}} \int_0^{2\pi} d\phi \int_0^{\frac{\pi}{2}} R'(\theta) \cdot \sin\theta d\theta = \int_0^{\frac{\pi}{2}} 2\pi \cos\theta \sin\theta d\theta \cdot \phi_{\text{phd}} = \pi \cdot \phi_{\text{phd}} \quad (7)$$

Since the photon flux,  $\Phi$ , is known, the External Quantum Efficiency (EQE) conversion is straightforward. The EQE itself is described as: "The ratio of photons that escape the LED into the forward hemisphere to the number of electrons flowing in the external circuit" [22]. So, the EQE unit is photons  $\cdot e^{-1}$  and is obtained with the following equation:

$$\text{EQE} = \frac{\Phi}{\frac{I_{\text{LED}}}{q}} \quad (8)$$

Where  $q$  is in the elementary charge of an electron:  $q = 1.602176634 \cdot 10^{-19}$  Coulomb.

The human eye has a specific response to light and is called the photopic factor  $P(\lambda)$ . However, the human eye is also sensitive to wavelengths  $< 390$  nm and  $> 720$  nm, the sensitivity factor is deficient in

those regions. Therefore, visible light for humans is considered between 390 and 720 nm<sup>[25]</sup>. The responsivity curve is shown in 9.

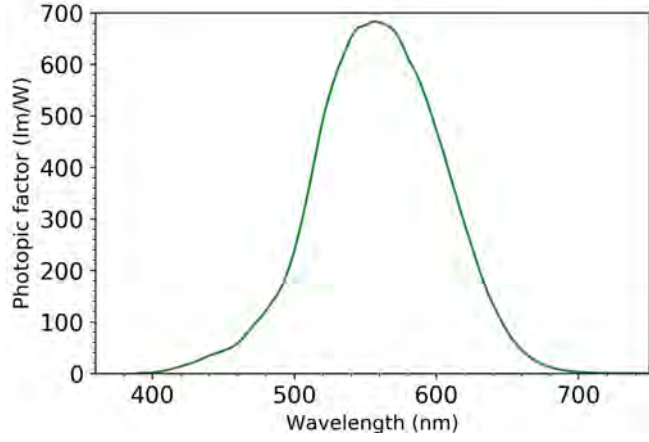


Figure 9: Photopic factor from the human eye as function of wavelength. Here is shown that the optimum is around 555 nm which is in the green regime (515-570 nm)<sup>[22]</sup>.

To consider the perception of light by the human eye in the visible region, the EL spectrum  $S(\lambda)$  from the LED has to be multiplied by the photopic function  $P(\lambda)$  and their respective energies and then weighed again by the EL spectrum. In order to get the last conversion factor called  $K$  9<sup>[22]</sup>, to calculate the luminous intensity ( $L'$ ) in candela (cd) and the luminance ( $L$ ) in candela per area ( $\text{cd}/\text{m}^2$ ).

$$K = \frac{\int P(\lambda) \cdot S(\lambda) \cdot \frac{hc}{\lambda} d\lambda}{\int S(\lambda) d\lambda} \quad (9)$$

Where  $h$  is Planck's constant  $c$  is the speed of light and  $\lambda$  the wavelength of the emitted light.

The last characterization step in this derivation is to use  $K$  to calculate  $L'$ . From this point it is now possible to convert  $L'$  into luminance ( $L$ ), the current efficacy ( $\eta_{CE}$ ) and the luminous efficacy ( $\eta_{LE}$ ). These equations are shown in equations 10 up to 13 below.

$$L'(\text{cd}) = \Phi_{\text{phd}} \cdot K \quad (10)$$

$$L(\text{cd}/\text{m}^2) = \frac{L'}{A_{\text{LED}}} \quad (11)$$

$$\eta_{CE}(\text{cd}/\text{A}) = \frac{L'}{I_{\text{LED}}} \quad (12)$$

"The unit candela has great historical significance. All light intensity measurements can be traced back to the candela. It evolved from an older unit, the candlepower, or simply, the candle. The original, now obsolete, definition of one candela was the light intensity emitted by a plumber's candle."<sup>[25]</sup>

$$\eta_{\text{LE}}(\text{lm/W}) = \frac{\pi \cdot L'}{I_{\text{LED}} \cdot V_{\text{LED}}} \quad (13)$$

Maximum efficiency values for MAPbBr<sub>3</sub> have been reported between 2014 and present with values:  $\approx 5 \cdot 10^{-3} \text{ cd} \cdot \text{A}^{-1}$  up to  $42.8 \text{ cd} \cdot \text{A}^{-1}$  [26],[7]. Moisture, water, oxygen and light cause the perovskite to degrade over time. Compared to other perovskite compositions, MAPbBr<sub>3</sub> has significantly lower efficiencies. However, it is relatively stable under ambient conditions. That is why in this work MAPbBr<sub>3</sub> is used to show a prove of concept that nanophotonic manipulation is possible at the MAPbBr<sub>3</sub> layer without damaging the MAPbBr<sub>3</sub> layer. Many reported EL peak values for MAPbBr<sub>3</sub> are between mostly 530 – 540 nm with a full width half maximum (FWHM) between 15 – 25 nm [26],[7].

Due to size control, tunability of the bandgap, and control of the halides' doping ratio, the whole visible spectrum can be realized. Perovskites emit photons with a narrow PL bandwidth which leads to high color purity [4]. Compared to conventional semiconductor materials, perovskites have significantly higher color purity. Nowadays the colour gamut for OLEDs is  $\approx 100\%$  of the NTSC (North American National Standard Committee). Quantum dot technology possesses a  $\approx 120\%$  NTSC and perovskites have achieved a 130 – 140% NTSC colour gamut. This results in enhanced accuracy in depicting colours and increased vividness in displays [4].

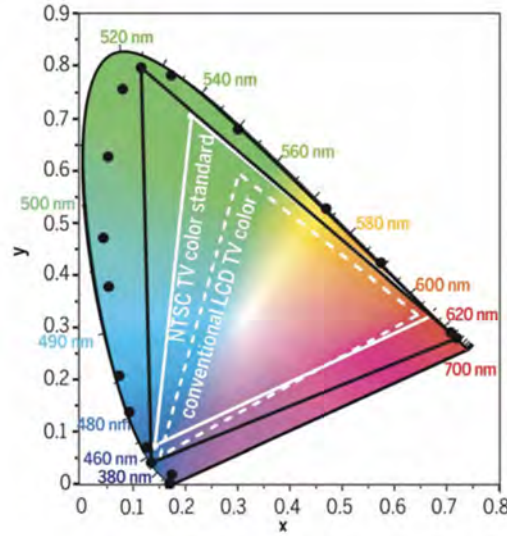


Figure 10: CIE colour scheme with PL spectra from perovskites versus NTSC colour standard and conventional LED TV colours. The black lines indicate the perovskite colour gamut [4].



### 2.3 TOTAL INTERNAL REFLECTION PROBLEM AND OUTCOUPLING ENHANCEMENT VIA NANOPATTERNS

In general, the efficiency of any LED is limited by nonradiative recombination (electrons and holes recombine without releasing a photon) and light trapping when there is radiative recombination<sup>[9]</sup>, <sup>[8]</sup>. In planar organic LEDs (OLEDs), around 70 to 80 per cent of the generated light is not outcoupled due to total internal reflection<sup>[9]</sup> (explained below). Zhao and colleagues simulated perovskite bulk heterostructures with that same values. Here they showed that only 20-25 per cent of the generated light is outcoupled<sup>[8]</sup>. This simulated illustration is already shown in the introduction in figure 1. The most significant fraction is lost as waveguide modes. These modes cannot escape the planar slab because the perovskite has a relatively high refractive index compared to the material aside from the perovskite slab and is reflected back into the perovskite. This is total internal reflection (TIR). From a conventional optical perspective, the phenomenon TIR occurs when a generated photon is emitted and directed under an angle. This is schematically shown in figure 11. When this angle is larger than the critical angle, the generated photon cannot escape and will be reflected inwards. These critical angle properties are dependent on refractive indices. So, in the case of the PeLEDs, this effect will be very present due to the relatively high refractive indices of perovskite material <sup>[8]</sup>,<sup>[9]</sup>.

*What is the problem?*

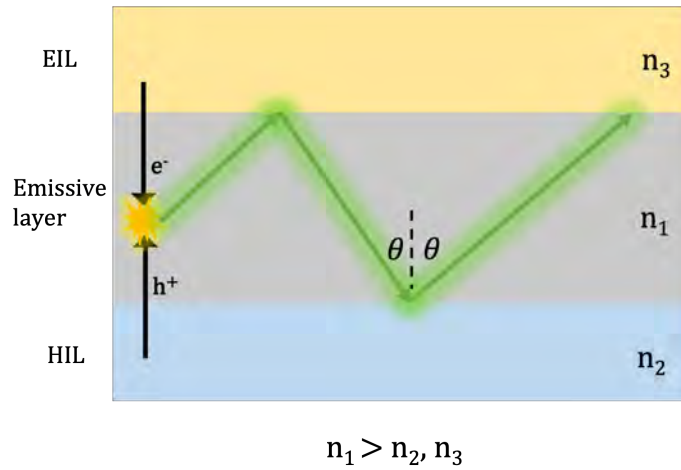


Figure 11: Waveguiding from conventional optical perspective

Therefore, to decrease waveguide modes in the emissive layer, the surface will be manipulated by fabricating nanopatterned MAPbBr<sub>3</sub> on top of the flat emissive layer. To make nanopatterned MAPbBr<sub>3</sub>, solgel is spincoated in between the HIL and the MAPbBr<sub>3</sub>. This is shown schematically in 12. In this work, the idea is that the perovskite



layer will follow the patterned structure in order to make a patterned emissive layer. Patterning perovskites itself is not a new idea. In solar cell applications, patterning perovskite has been done before<sup>[27],[28]</sup>. There are many ways to fabricate these perovskite nanostructures. Laser ablation, CVD and chemical synthesis are examples of making these nanoparticles<sup>[28]</sup>. Also, the use of soft lithography on not completely crystallized perovskite has been shown in research<sup>[27]</sup>. This thesis deviates from this earlier work because the perovskite layer does not undergo any other procedure than spincoating because there is already a pattern. This is due to the stamping of the already present and solgel.

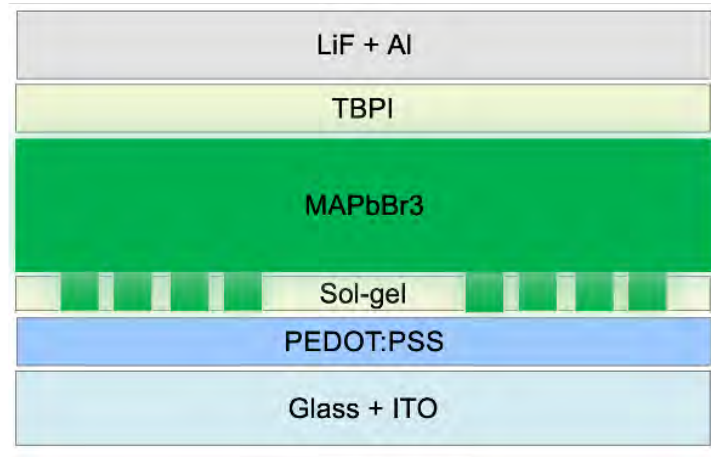


Figure 12: Absorption spectra and photoluminescence

The  $\text{MAPbBr}_3$  has a high refractive index and is a dielectric material with dielectric resonant properties. When the dimensions are in the range of 200-1000 nm, the physics of meta-optics with Mie-type modes arise. The nanostructures can achieve resonant response and sub-wavelength light localization<sup>[28]</sup>. Mie-theory describes Mie-type resonances, but one is mostly interested in the low-order resonant modes for this work. The first mode is a magnetic dipole when the wavelength of the light over the refractive index ( $n$ ) becomes comparable with the particle dimensions<sup>[28]</sup> (see equation 14). Now the electric field polarization is antiparallel at the opposite boundaries of the nanostructures. The lower order modes results in coupling to the rotating displacement currents with the magnetic field oscillating in the centre. Higher-order modes are used to enhance this light-matter phenomenon and enhanced near-field densities inside these dielectric nanostructures, which enhance the number of electromagnetic waves inside the structures<sup>[28]</sup>. Tingutseva et al. showed light-emitting perovskite nanostructures with enhanced PL due to this exciton coupling to Mie resonances<sup>[29]</sup>. Aside from this enhancement, in terms of conventional optics, there is also the effect of breaking surface geometry

due to the patterned MAPbBr<sub>3</sub>. The angle of incidence with the top boundary will be different due to these patterns what will lead to a larger escape cone<sup>[27],[30]</sup>.

$$D_{\text{res}} \approx \frac{\lambda}{n} \quad (14)$$

In order to simulate the dimensions of such a nanopattern, one can make use of the reciprocity principle<sup>13</sup>. This states that the far-field emission from the metasurface with emitters is reciprocal to the intensity of the near-field excited in the metasurface by an incident plane wave. So, basically, for simulating an optimized outcoupling pattern, the absorption in the incoupling simulation needs to be maximized<sup>[30]</sup>.

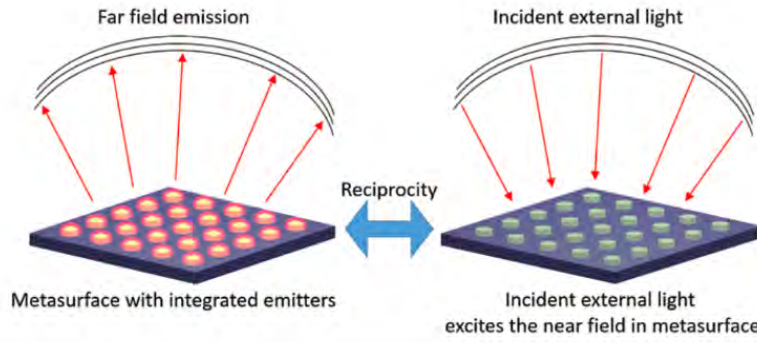


Figure 13: On the left a metasurface with emitters is for simulation calculation the same as incident external light that excites the near field in the metasurface<sup>[30]</sup>

## 2.4 SOFT COMFORMAL IMPRINT LITHOGRAPHY (SCIL)

For making nanopatterned structures with the MAPbBr<sub>3</sub> emissive layer, a form of soft lithography is used that combines the advantages of rigid stamps: good resolution, low pattern distortions and the low-costs; with wafer-scale patterning from soft stamps that have a long stamp lifetime<sup>[31]</sup>. SCIL has been used to fabricate photonic crystal LEDs, three-dimensional photonic structures and more. To achieve wafer-scale conformal contact under relatively low pressure, the SCIL technique uses a stamp composed of two rubber layers on a thin glass support, see figure<sup>[31]</sup>. The nanopatterns are moulded in a thin layer made from a stiff silicone rubber, which is called X-PDMS and is supplied by Philips, which allows for accurate replication of nanometer-sized structures<sup>[31]</sup>.

The high and low modulus terms in figure 14 are Young's modules. Young's modulus describes properties of a solid undergoing tension

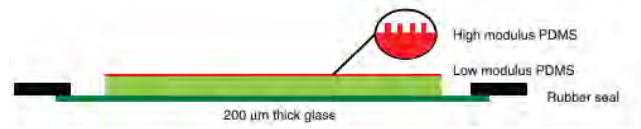


Figure 14: Schematic of a SCIL stamp where the thin glass holds the two-layer silicone rubber stamps. The high-modulus PDMS layer (red) is X-PDMS and contains the patterns. The low modulus (light green), helps to make better contact with the surface.<sup>[31]</sup>

in the elastic region and returns to its original shape<sup>[32]</sup>. This means for the pattern that when the material is stiffer, the Young modulus is steeper/higher but bends back to the original pattern. So, in the SCIL stamps: the upper layer is stiffer than the low modulus PDMS. This gives good properties to bend the stamp out of plane. PDMS itself is a transparent glass-like silicon polymer with properties suited for bending without breaking<sup>[31]</sup>.

The thin glass is flexible in the out-of-plane direction, which allows conformal contact as well to be made over wafer-scale areas. Nevertheless, also stiff in in-plane directions, which prevents pattern placement distortions. The modulus of the X-PDMS can reach a very high stiffness but still makes conformal contact as the whole stamp is flexible on varying length scales from micro to centimetre scale<sup>[31]</sup>.

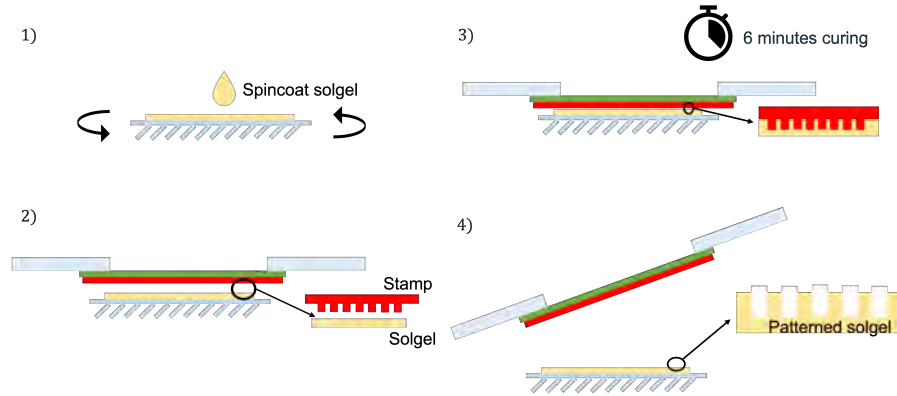


Figure 15: 1) Solgel spincoated on top of ITO/PEDOT:PSS. 2) The SCIL stamp is directly placed on top of the solgel. 3) The solgel needs to cure for 6 minutes in order to make proper patterns. 4) After 6 minutes the stamp can be removed smoothly and the solgel will be left with nanostructures. *This illustration is based on the Verschuren article<sup>[31]</sup> and adjusted to this work's application.*

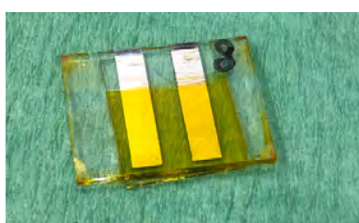
## METHOD SECTION

The next chapter presents the experimental techniques used for this study. **Note:** When the cleanroom is mentioned, the AMOLF Nanolab Amsterdam is meant. This Nanolab is an ISO-class 7 cleanroom. The PeLEDs were fabricated and analysed partially here. The chemistry was carried out in the benches in the cleanroom with an ISO-class 6 classification.

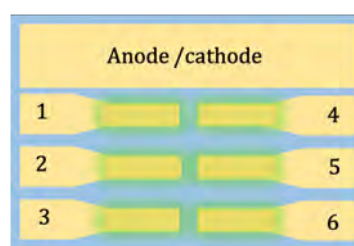
### 3.1 FABRICATION PELEDs

#### 3.1.1 Substrate and Cleaning

The glass substrates are pre-patterned with ITO ( $\pm 100\text{nm}$ ) with a total thickness of  $1.1\mu\text{m}$ . The substrate size is  $20 \times 15\text{ mm}$  with 6 pixels with a pixel area of  $4.5\text{ mm}^2$ . The pixels are highlighted green in figure 10. In addition to the pixels, an anode and cathode strip are placed at the substrate's top. The ITO is fully oxidised, and the resistivity is  $20\ \Omega/\text{square}$ . The glass substrates covered with ITO were cleaned in acetone, distilled water and isopropanol consecutively in an ultrasonic bath of each 30 minutes in the cleanroom. Afterwards, the substrates were dry gunned with a nitrogen gun and, when dry, were placed in a plasma etcher (Oxford Plasmalab 80+) for an oxygen descum clean for 1.30 minutes at vacuum pressure below  $1 \cdot 10^{-6}$ . The plasma etching cleaned the substrates and increased wettability (more hydrophilic) for spincoating later on in the process.



(a) PeLED after encapsulation



(b) schematic overview pixels

Figure 16: Real and schematic view from a perovskite LED substrate.

**Note:** The  $\text{MAPbBr}_3$  precursor fabrications and spincoating processes are carried out in a glovebox filled with nitrogen. In the glovebox, the oxygen levels are below 10 ppm and the water levels below 1 ppm to avoid material degradation.

### 3.1.2 Precursor Fabrication & Other Materials

First,  $\text{PbBr}_2$  powder (Sigma Aldrich) was weighted in a vial and Dimethylsulfoxide (DMSO) is added to get a solution of 1.5 M solution. The solution is stirred on a hotplate at  $100^\circ\text{C}$  for half an hour at 500 rpm to dissolve the solution completely. Afterwards, the solution is cooled off until room temperature is reached. Second, MABr (TCI) was weighed into a second file, and  $\text{PbBr}_2$  was added into this second file to obtain a solution of 1.1 M of  $\text{MAPbBr}_3$ . The methylammonium was stirred at  $60^\circ\text{C}$  for 24 hours at 500 rpm in order to dissolve the perovskite completely.

Finally, the antisolvent precursor used in this work was chlorobenzene (Sigma Aldrich) mixed with 0.1wt% of TBPi (Ossila) to ensure a homogeneous thin film of perovskite crystals. This antisolvent precursor was also fabricated inside the glovebox. The PEDOT:PSS was bought ready for usage from Ossila. The PEDOT:PSS version used was the AI 4083 and needed to be stored at  $5-10^\circ\text{C}$  in a laboratory refrigerator outside the glovebox. Furthermore, TBPi, LiF and Al used for evaporation were stored in a dry glovebox. There is no chemistry taking place in the dry glovebox to avoid cross-contamination except for a closed thermal evaporator system.

### 3.1.3 Spincoat Processes

#### 3.1.3.1 PEDOT:PSS

Directly after the glass substrates were cleaned, PEDOT:PSS was spincoated in the cleanroom. The spincoat speed was 1500 rpm with an acceleration of 1500 rpm/s for 12 seconds and increased to 3000 rpm with an acceleration of 1500 rpm/s to create a uniform layer and directly annealed at  $220^\circ\text{C}$  for 10 minutes. After spincoating, a PEDOT:PSS layer with a thickness of 65nm was left. After annealing, the substrates were cooled on a copper plate to room temperature and again plasma cleaned. The cleaning/etching happened in the Diener Electronic Pico QR-200-PCCE, which is used for plasma cleaning non-metals with  $\text{O}_2$  gas. Short oxygen clean of 40 seconds removed 10-15 nm of PEDOT:PSS and a clean layer of  $\pm 50\text{ nm}$  was left.

**Extra step for patterned devices only, otherwise skip this part and go directly to 3.1.3.3.**

#### 3.1.3.2 Solgel & SCIL

The solgel T1100 (SCIL nanoimprint technologies) was taken out of the refrigerator at least 30 minutes before the spincoating procedure started (also in the cleanroom). This was done to ensure that the sol-

gel solvents did not vaporize too fast. The spincoater inner lid was mounted, and a fragile layer of solgel was spincoated on top of the PEDOT:PSS. In order to prevent the salty PEDOT:PSS to dry out the layer of solgel that needed to be patterned. The acceleration was 2000 rpm/s for 2 seconds until 4000 rpm was reached and continued spinning at 4000 for 15 seconds. The substrates were taken out of the spincoater and cured for 30 minutes to ensure that the solgel was completely dry. Again, the substrates were placed inside the Pico plasma cleaner for another etch to increase hydrophilic surface cohesion between surfaces, same procedure as in 3.1.3.1.

The inner lid was still mounted in the spincoater, and the substrates were placed in the spincoater directly after etching. The solgel is now spincoated at 1500 rpm with an acceleration of 1500 rpm/s for 10 seconds. When the procedure finished, the substrates were directly imprinted with the SCIL wafer and pressed for  $\pm 20$  seconds on all sides to ensure the pattern was properly printed into the solgel. The SCIL pattern stayed imprinted for 6 minutes so the solgel could cure.

To recombine electrons and holes, solgel between the structures needed to be etched away. Therefore, in the Plasma80+, a solgel etch was carried out. This solgel etch is an etching with a combination of argon and CHF<sub>3</sub> gas for 3.40 minutes. Also, a powerful O<sub>2</sub> etch was carried out for 3 seconds to etch into the PEDOT:PSS and clean the surface. The pressure was again below  $1 \cdot 10^{-6}$ . Afterwards, to clean the substrate and to increase wettability, the substrate was placed in the Pico for an oxygen descum for 1 minute under a pressure of 0.20  $\pm$  0.05 mbar. This sequence left a substrate with ITO (100 nm)/PEDOT:PSS (45  $\pm$  5 nm)/patterned solgel structures. The substrates were ready to be moved to the glovebox for the next layer.

### 3.1.3.3 MAPbBr<sub>3</sub>

The substrates were moved directly into the glovebox to have no interaction between oxygen and MAPbBr<sub>3</sub>. The substrates were placed in the middle of the spincoater. 180  $\mu$ L of MAPbBr<sub>3</sub> precursor solution was deposited on the substrates. A two-step deposition method was used. The acceleration was 500 rpm for 6 seconds until 3000 rpm was reached and stayed at 3000 rpm for 45 seconds. Afterwards, the spincoating stopped, and 300  $\mu$ L chlorobenzene + 0.1 wt% TBPI was deposited directly under an angle on the substrate, and the spincoat sequence started again. After spincoating, the substrates were annealed at 100 degrees on the hotplate for 1 hour. A transparent and homogeneous perovskite orange layer occurred.

### 3.1.4 Thermal Evaporator

The thermal evaporator used in the device fabrications was the Angstrom engineering 6-source evaporator. TBPI, LiF and Al were all sublimed in a vacuum with pressures below  $2 \cdot 10^{-6}$  mBar. After moving the substrates from the chemical glovebox to the evaporator glovebox (the glovebox where no liquid chemistry is performed), the anode/cathode strips were cleaned with a surgical knife. The TBPI (Ossila) was refilled before every evaporation at a rate of  $0.5 \text{ \AA/s}$  under 20% rotation. Until a thickness of 40 nm was reached. Consecutive, LiF (Sigma Aldrich) was refilled once a month. LiF was evaporated at a rate of  $0.05 \text{ \AA/s}$  until 20% rotation until a thickness of 1.2 nm was reached.

At last, the aluminium back contact was thermally evaporated at a rate of  $0.5 \text{ \AA/s}$  without rotation until a thickness of 70 nm was reached. Three Al pallets were used for evaporation on an evaporation boat made explicitly for Al. Due to incompatibility problems between Al and materials used in standard deposition boats. While melting the Al, surface tension of the liquid metal wick up the boat, and when the evaporation is done, the lower surface tension causes it to recede and stressing the walls of the boat with cracked boats as consequences. Also, the aluminium can move up the copper posts and could cause a short. Therefore, proper settings for thermally evaporating Al are a necessity.

*The substrates are moved to another glovebox where the devices were allowed to be encapsulated.*

#### 3.1.4.1 Encapsulation

Encapsulation is done with epoxy material (E132 Ossila) that is used as an adhesive for LED and PV applications. This epoxy can be applied without damaging polymers of cathode materials. Three to four droplets of epoxy were deposited on top of the Al. After that, a cover glass (Ossila) with dimensions made explicitly for the substrates was placed on this epoxy. The whole stack was then placed under a UV lamp at a wavelength of 365 nm for 45 minutes to cure the epoxy. The encapsulation, including coverglass, provided the substrates with protection against oxygen and water degradation.

A second way of encapsulation was used in this work. This was done with an adhesive gel/epoxy material that can be bought commercially and is called "Blufixx". This method comparable with the upper method only the material is different and the LED on the back of the "Blufixx" cured the epoxy within seconds.



#### 3.1.4.2 *Final Cleaning*

Once the substrates were encapsulated, the stack is finished, and the substrates are now full PeLED devices. The devices were taken outside the glovebox. Here, the sides of the devices were cleaned with a surgical knife first and then cleaned with IPA on a cotton swab to improve connectivity. Also, the substrate back was cleaned properly with the surgical knife and IPA to have the clearest glass site up. At this stage, the devices were ready to be measured for JVL measurements.

### 3.2 CHARACTERIZATION MEASUREMENTS

This section presents a descriptive way of how the PeLEDs' performance was measured with JVL measurements. Also, individual layer qualities were characterised using UV-Vis, XRD, SEM and AFM.

#### 3.2.1 *JVL measurements*

**OLED Lifetime System (Ossila)** was used to measure JVL. The main components of the system are a source measure unit and a specially designed photodiode lid. It has an automated test board that can switch between pixels without user intervention. So 6 pixels can be measured consecutive after each other. The PeLED devices are secured in the lid compartment in the test board. This specially designed photodiode is placed in the lid so that the photodiode is right above the devices. The two SMUs can work at the same time during operation. One measures JV with the test board, and the other measures the photodiode current. The raw data, as earlier mentioned in 2.2.3, are  $V_{LED}$ ,  $I_{LED}$  and  $I_{phd}$ . All PeLEDs were tested with a voltage sweep between -0.5 - 7.5 V. The sweep delay was set on 0.1s, and the voltage increased in steps 0.025 V. The resolution setting for the  $I_{LED}$  was 4096. The resolution setting for the  $I_{phd}$  was 16384.

#### 3.2.2 *Thickness, roughness and surface morphology*

**AFM - Bruker Dimension Icon:** Atomic force measurements were carried out. Both to analyse surface morphology from spincoated and thermally evaporated layers and analyse the layers' thickness by making scratches in the layer with a sharp tweezer and measuring the step height in an AFM scan. The measurement used a tapping mode AFM with a ScanAsyst-air probe.

**SEM - FEI Helios 600 DualBeam:** Scanning electron microscopy was carried out to analyse PEDOT:PSS, MAPbBr<sub>3</sub> and total stack thicknesses and surface morphology. This was obtained by mounting sam-



ples horizontal and by mounting devices under an angle of  $45^\circ$  so that a cross-section could be carried out. For the cross-section, devices were cut with a cleave set in the cleanroom and residuals were blown off with an  $N_2$  gun. The SEM operated between 3.0 - 10 kV with a beam current of 43 - 86 pA.

**Profilometer - KLA Tencor stylus profiler P7:** Profilometer measurements were carried out to analyse layer thicknesses. PEDOT:PSS, PVK and MAPbBr<sub>3</sub> were scratched after spincoating with sharp tweezers. A calibrated needle moved along the substrate's surface and measured differences in height precisely in vertical directions. The applied scan speed was between 20 - 50  $\mu\text{m/s}$ , and the applied force was between 0.5 - 2 mg.

### 3.2.3 XRD, UV-Vis and PL

**XRD - Bruker D2 Phaser:** X-ray diffraction measurements were carried out using a Bruker D2 Phaser. This setup uses a Cu K $\alpha$  tube to generate X-rays. The X-rays were incident on the substrate under variable angle  $\theta$ . These X-rays were diffracted by the substrate and generate constructive interference according to Bragg's law. The detector was positioned at angle  $\theta$  and detected the x-ray intensity at each incident angle, opposite the normal compared to the detector. Peaks at specific positions were characteristic for crystallisation properties. So, it is possible to identify a crystal from its XRD peaks. For MAPbBr<sub>3</sub>, the only peaks that were usually observed were the (001), (002) and (003) plane peaks at  $2\theta = 15^\circ$ ,  $30^\circ$  and  $45^\circ$ , respectively. Three runs between  $10^\circ$  and  $60^\circ$  were enough to get clear peaks. The increment used was  $\pm 0.02\theta$  per step with a step-time of 0.1s. The scan mode was a continuous PSD scan.

### UV-Vis - LAMBDA 750 UV/Vis/NIR Spectrophotometer, Perkin Elmer:

UV-vis measurements were carried out to measure steady-state absorbance spectra. The spectrophotometer is equipped with a deuterium lamp and a tungsten lamp, allowing for an excitation wavelength range between 250 and 800nm, an InGaAs detector, and an integrating sphere. The substrate is positioned in the integrated sphere. The light hits the substrate and absorbs a fraction of the light, reflects (R) and scatters (S) a fraction and transmits the residual (T). The substrate was positioned under an angle  $\pm 12^\circ$  compared to the incident beam, causing the reflected light to be distributed into the integrating sphere along with the transmitted and scattered light. A detector at the bottom of the integrating sphere collects the light and compares this with a calibrated reference measurement. From this data, Tauc approximations were used to calculate bandgap values.

**Electroluminescence - Ocean Optics USB4000:** The electroluminescence measurements were measured by using the JV system of the OLED Lifetime System with an open lid. On top of this, a photoluminescence spectrometer was used to collect the EL spectrum of the PeLEDs at 6 V. The software used was Switchboard Control. The integration time was set at 500 ms. As reference, a dark background measurement was made before 5 EL measurements were carried out, averaged, and normalised to obtain the EL from the PeLEDs device.

#### 3.2.4 *Measurements for Simulation*

**Ellipsometer - Ellipsometer VB-400 J.A. Woollam:** Variable Angle Spectroscopic ellipsometry (VASE) is carried out to obtain n- and k-values which describe the refractive indices from materials. In this work, SE is used to determine refractive indices from PEDOT:PSS and MAPbBr<sub>3</sub>. The ellipsometer is first calibrated before measurements were carried out. The Brewster angle was for both around  $\pm 69^\circ$  and between  $63^\circ$  -  $75^\circ$  was used as an interval with  $3^\circ$  increment steps. The slit width was 1800  $\mu\text{m}$ , and the dynamical averaging mode was performed. The software used for modelling n- and k-values was CompleteEASE from J.A. Woollam Co. Customers version 4.78. Fitting measurements for the PEDOT:PSS model was done with a Gaussian harmonic oscillator ( $\text{MSE} \approx 5.7$ ), and fitting and modelling MAPbBr<sub>3</sub>, a Cody-Lorentz model was used in combination with a Gaussian ( $\text{MSE} \approx 37$ ).



## RESULTS EN DISCUSSION

First, the flat devices were optimized and the results are presented. Second, the patterned results are presented. Afterwards, these results are compared to each other and everything will be discussed.

### 4.1 FLAT DEVICES

#### Results absorption, photoluminescence and electroluminescence:

The most important layer is the MAPbBr<sub>3</sub> emissive layer. The layer needs to be homogeneous and uniform without showing pinholes. Therefore, the MAPbBr<sub>3</sub> is characterized extensively. In figure 17 the absorption (green) is presented. A Tauc Approximation is used to approximate the bandgap energy based on the absorption graph. This approximation calculates the steepest slope and calculates the intersection with the absorption offset ( $\approx 0.0$ ). This result shows a bandgap value at 2.3 eV / 535 nm. Furthermore, earlier measurements of MAPbBr<sub>3</sub> photoluminescence at room temperature show a maximum at 535 $\pm$ 1 nm under 0.6 Sun for 1 second exposure time.

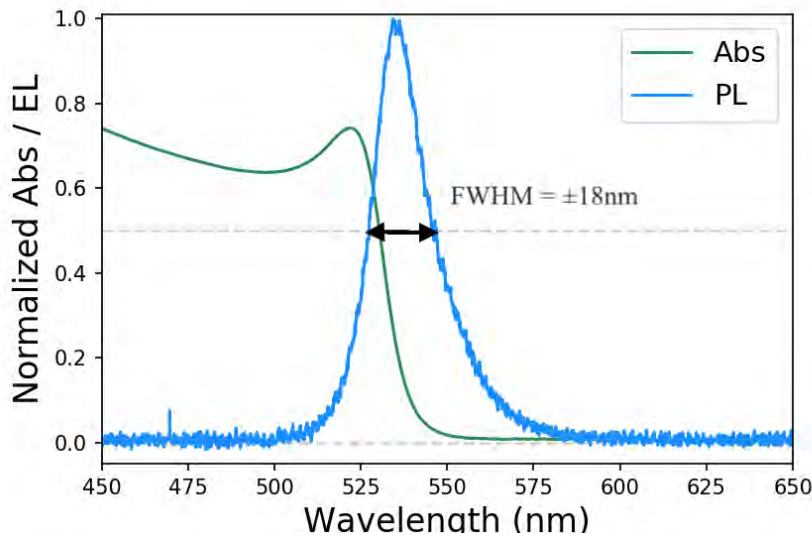


Figure 17: Absorption spectra and photoluminescence

The electroluminescence is also measured and showed earlier in the thesis and in figure 18 the photoluminescence and electroluminescence are plotted together. The Full Maximum Half Width (FMHW) is  $\approx 18$  nm. The dataset is already normalized and the this dataset is

used to find the two values closest to the 0.5 line. The graphs in figure 18 have major overlap. This means that the influence of the transport layers on the emission is low and the peak value is for both at 535 nm.

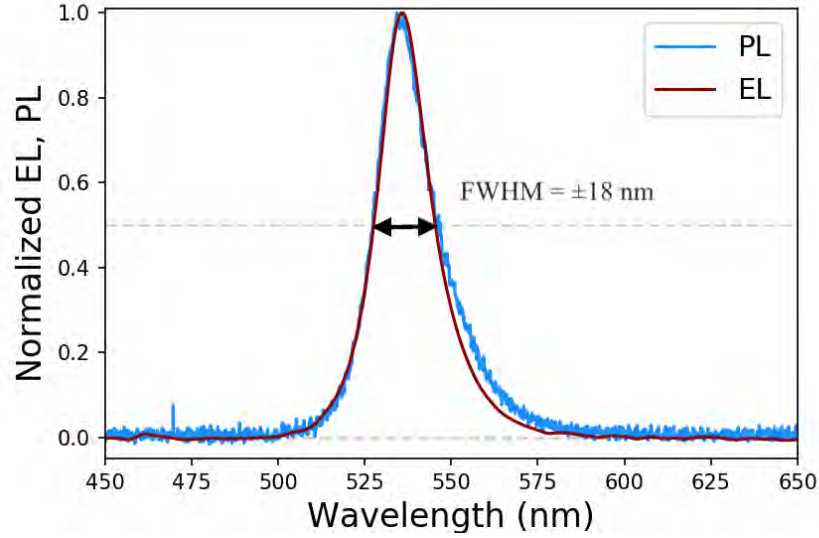


Figure 18: PL versus EL

The XRD of the MAPbBr<sub>3</sub> is presented below in figure 19. Characteristic peaks at 15°, 30° and 45° of MAPbBr<sub>3</sub> are shown<sup>[33]</sup>. Furthermore, no residual material peaks are witnessed. Excess PbBr<sub>2</sub> have characteristic peaks at 12° and multiples.

#### Grains and roughness results:

SEM imaging shows a small-grained homogeneous MAPbBr<sub>3</sub> layer without pinholes. These layers lighted up homogeneously under operation. This is basically the result of optimizing the MAPbBr<sub>3</sub> spincoat procedure until the emissive layer presented a transparent and clear surface. Earlier in this project, during optimization, the MAPbBr<sub>3</sub> turned non-transparent/ opaque during or after spincoating and showed different crystallization with grain sizes up to 5000 nm. These MAPbBr<sub>3</sub> layers did not light up under operation, showed inhomogeneous sparkling or just shorted the pixel and burned the MAPbBr<sub>3</sub>.

Surface morphology and low roughness are essential for high film quality. The AFM measurements present as well a homogeneous layer of perovskite material. The Root Mean Squared (RMS) of these layers was measured at 7.2 nm. From these AFM measurements, the distribution of grain sizes between 20 and 300 nm can be simulated. Most of the grains are distributed between 50 and 200 nm (Appendix). There has to be said, due to overlapping of grains in the AFM image,

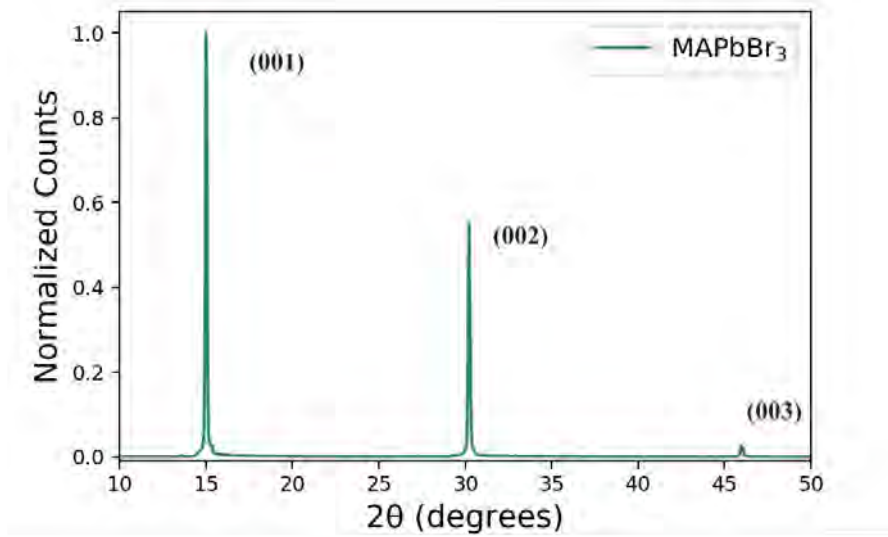


Figure 19: X-ray diffraction flat device with on the x-axis the degrees and on the y-axis the normalized counts.

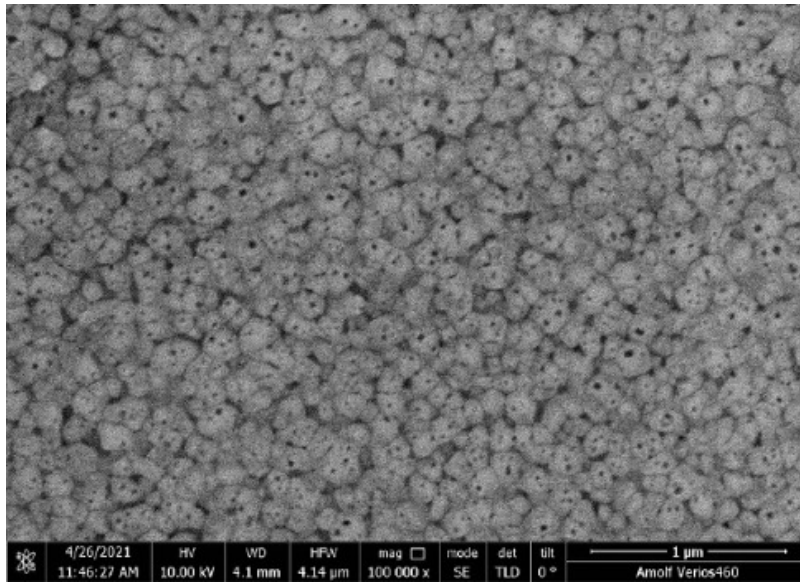


Figure 20: Scanning Electron Microscopy from MAPbBr<sub>3</sub> spincoated on top of ITO and PEDOT:PSS. Crystallization dimensions are relatively small (<200 nm)

that this is an approximation but that it supports the visual data from the SEM.

#### Current, voltage and luminance measurements:

The MAPbBr<sub>3</sub> layer is investigated, and now the full flat devices will be analysed under operation. As mentioned in the method section, voltage sweeps are carried out to see how the LED devices performed.

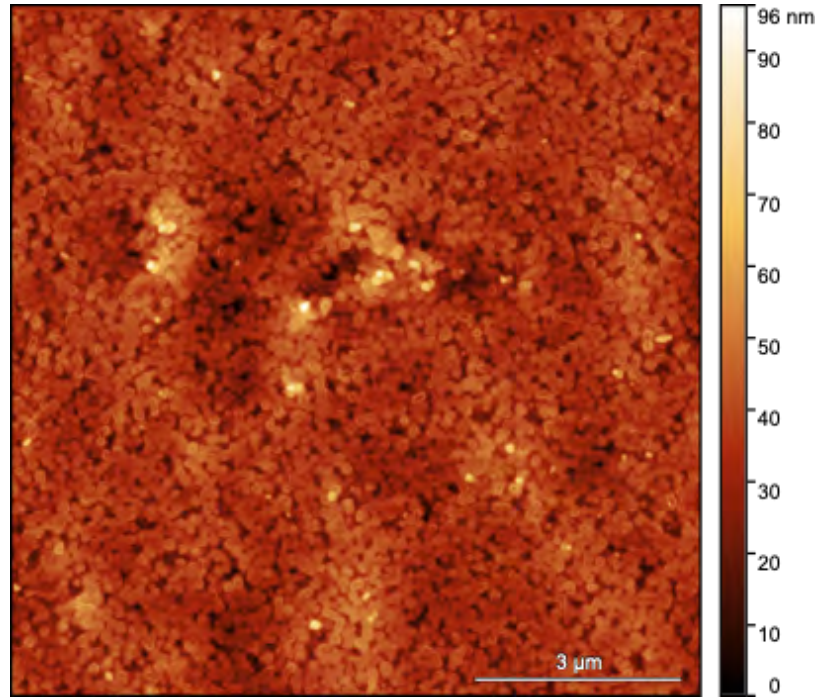


Figure 21: Atomic Force Microscopy of MAPbBr<sub>3</sub> spincoated and annealed on top of PEDOT:PSS. The dimensions of this AFM measurement is 10 x 10 μm in order to give an overview of the homogeneity of the emissive layer.

The sweeps ranged from 0 V up to 7.5 V in steps of 0.025 V and the current efficacy after data analysis was extracted. In figure 33a one sees a pixel lighting up homogeneously. In figure 33b, an example pixel is shown where you can see a turn-on voltage at  $\pm 3.0$  V. Furthermore, an optimum is shown at  $\pm 5.0$  V. In the efficacy curves, the PeLEDs show an optimum value between the turn-on voltage and 7.5 V. The PeLEDs saturated during the sweep and therefore the current efficacy decreases after a maximum value.

The distribution of the current efficacies are presented in figure 23. After optimising the flat devices, 53 pixels were fabricated in two batches of devices that lighted up homogeneously with the same fabrication procedure. The data points for the distribution are extracted at a maximum value between the turn-on voltage and 6.5 V and are plotted in a histogram. This histogram is fitted with a "normal distribution". The mean value is at  $15.8 \cdot 10^{-5}$  cd/A. The standard deviation is  $8 \cdot 10^{-5}$  cd/A. In the distribution histogram, the current efficacy is on the x-axis and on the y-axis is the probability of finding a specific current efficacy.

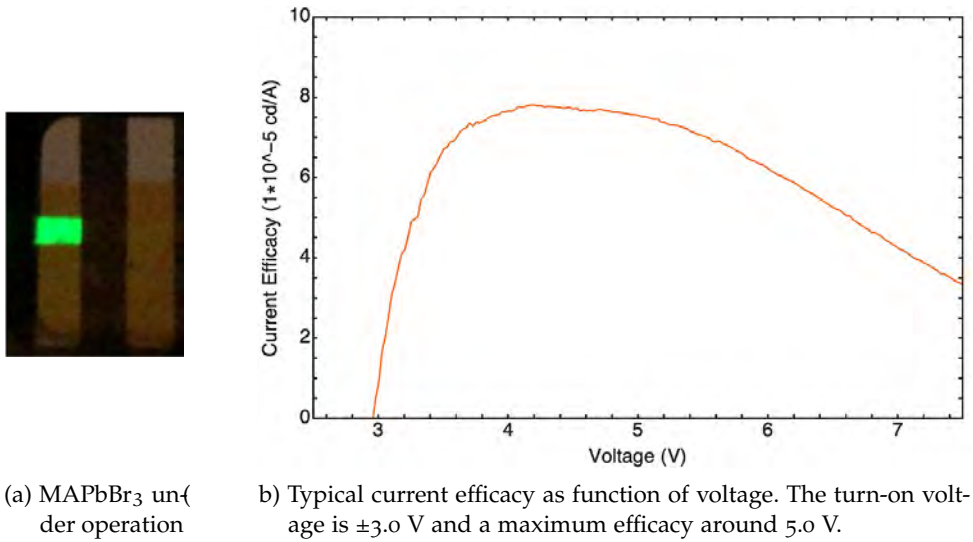


Figure 22: (a) Shows PeLED under operation at  $\pm 7.0$  V; (b) Shows example measure of pixel during voltage sweep.

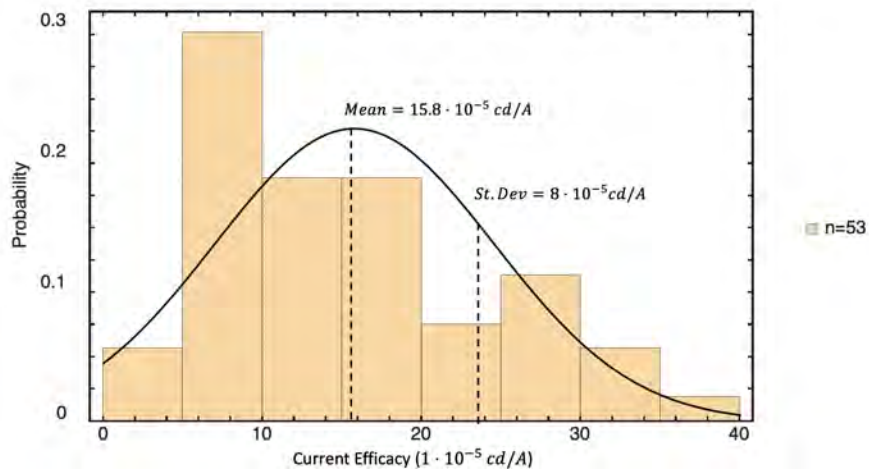


Figure 23: Current efficacy presented as a distribution of performance of flat devices.

## 4.2 PATTERNED DEVICES

### Simulation results:

Ellipsometry data from MAPbBr<sub>3</sub> is fitted to give  $n$  and  $k$  values for the simulation. The data is below. The refractive index is  $\approx 2.2 - 2.45$ , and a peak is seen near 535 nm. The extinction coefficient is going to zero after the drop around 535 nm. The figures can be found in the Appendix (34a)

**Note:** The simulated data and the pattern dimension simulation are carried out by Andrea Cordaro



In figure 24 simulated results for the flat device and optimised patterned device are presented in the blue line and dashed blue line, respectively. This is plotted together with the EL spectra measured from the optimised flat device. Between 490 nm and 540 nm, there is no significant difference between the flat and patterned devices. In the patterned device, an increased absorption is present between 540 and 550 nm. The flat device and patterned device simulations are weighted by the EL spectra to calculate the average increase in absorption between the two devices. The patterned device shows an absorption increase of  $\approx 3\%$ . Following the reciprocity principle, reciprocal to the incoupling, the outcoupling should also be enhanced with  $\approx 3\%$ .

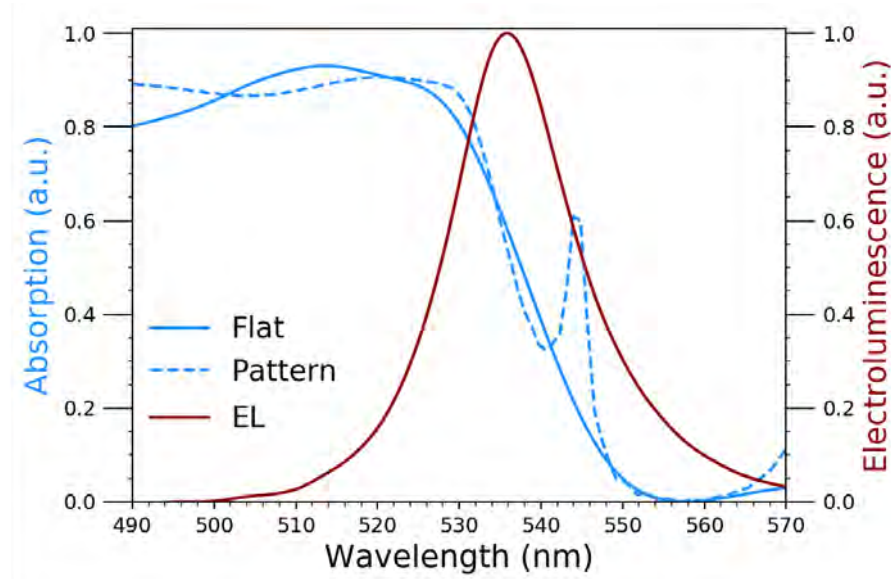


Figure 24: Simulated results for flat and patterned device plotted together with the by the EL spectra

The dimensions are of the optimised pattern is hexagonal with a period of 336 nm, a diameter of 220 nm and a height that was fixed at a maximum of 90 nm (see figure 25). It was fixed to prevent complications with the stamping procedure.

#### Stamping and etching results:

*In order of time, an older stamp is used to spare time that had dimensions close to the simulated pattern above. This pattern showed no significant difference from the simulated pattern. The period was 325 nm, the diameter was 280 nm, and the height was 125 nm.*

The solgel patterns are distributed homogeneous and uniform as can be seen in figure 26a and 26b. The dimensions are the same as initially

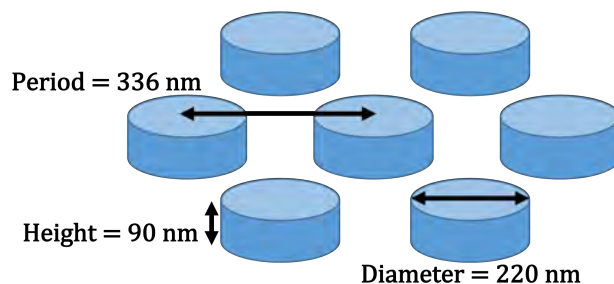
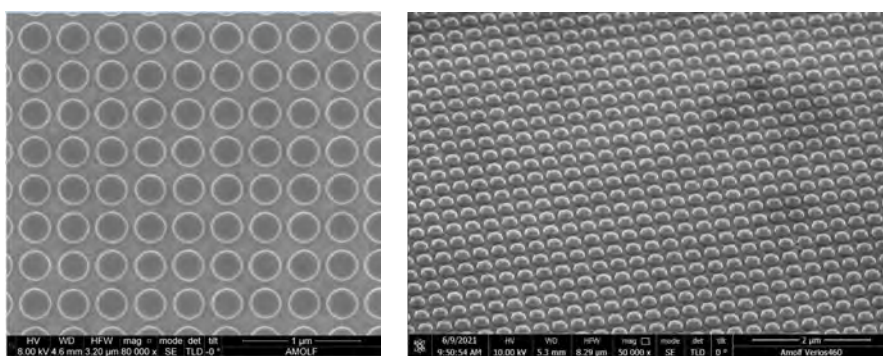


Figure 25: Simulated pattern dimensions

expected. This shows the precision of the SCIL technique.



(a) Unetched top view with 1 micron scalebar

(b) Unetched angular view with 2 micron scalebar

Figure 26: Unetched solgel on top of PEDOT:PSS and ITO

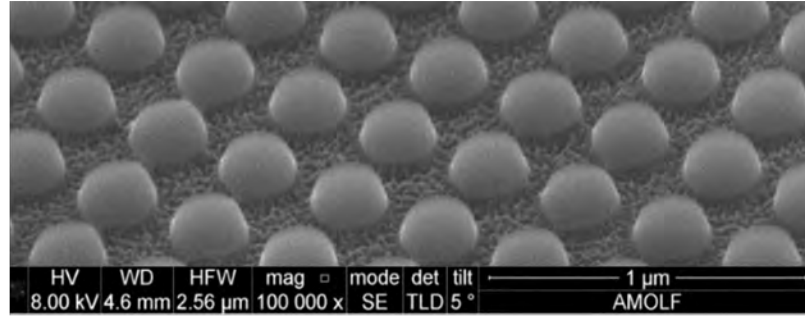
To be able to make contact between the HIL and  $\text{MAPbBr}_3$  the solgel in between the structures is etched away as described in the method section above (3.1.3.2).

On the left side can be seen that the solgel is etched away between the structures. The cross section shows the pattern on top of the PEDOT:PSS, the ITO and glass.

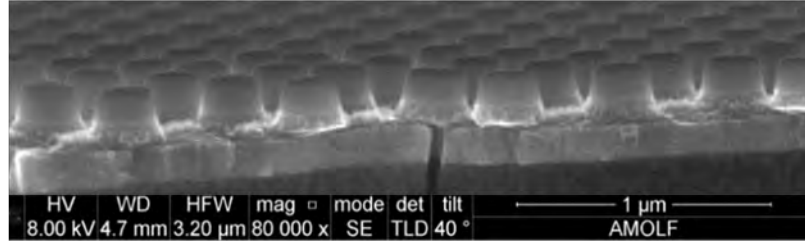
#### Perovskite + patterning results:

After spincoating the perovskite layer on top of these nanostructures the perovskite crystallization is measured with XRD. The XRD shows again peaks at  $15^\circ$  and multiples without excess precursors peaks.

The patterned PeLEDs showed recombination of electrons and holes under operation, and green photons were again emitted. The emission can be seen in figure 29a and was less uniform than the flat devices. SEM images showed in 29b how the perovskite crystallized on top of the patterns. Voids can be detected between the structures instead of homogeneous filling between the solgel structures at cer-



(a) Etched angular view with 1 micron scalebar



(b) Cross section etched substrate 1 micron scalebar

Figure 27: The glass substrate at the bottom stacked with ITO layer ( $\pm 100\text{nm}$ ), PEDOT:PSS layer ( $\pm 40\text{-}50\text{ nm}$ ) and the solgel nanopatterns on top.

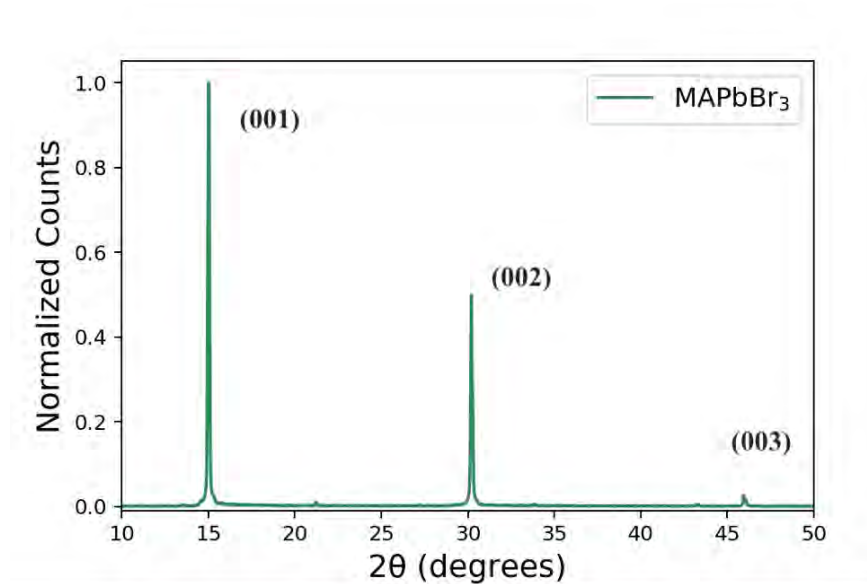


Figure 28: XRD patterned device crystallized on top of ITO and PEDOT:PSS

tain places.

One of the possible options to solve these voids was to heat the precursor solutions at  $60^\circ$  Celsius. This is the temperature where  $\text{MAPbBr}_3$  precursors are fabricated. By heating the precursor solution, the solution's viscosity dropped, and SEM images showed more cohesion

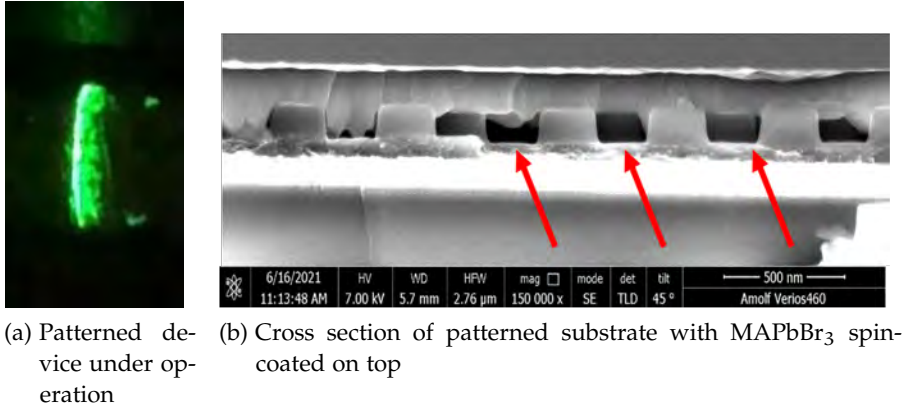


Figure 29: The glass substrate at the bottom stacked with ITO layer ( $\pm 100$  nm), PEDOT:PSS layer ( $\pm 40$ -50 nm) and the solgel nanopatterns on top

between the PEDOT:PSS and the MAPbBr<sub>3</sub> (see 30).

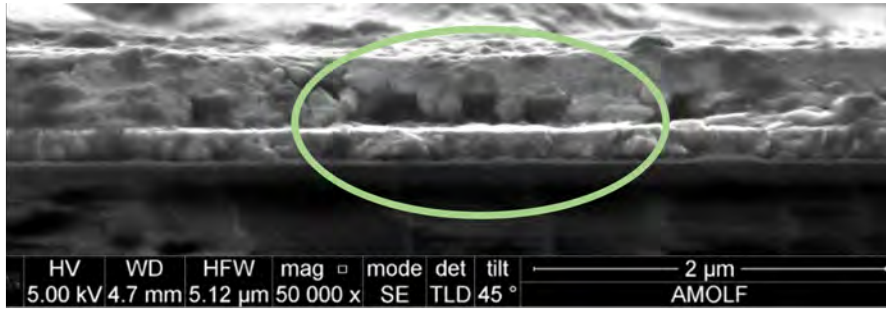


Figure 30: SEM of heated precursor solution before spincoat procedure.

Finally, 29 pixels are fabricated that lighted up. The efficacy was fitted with a normal distribution, and the mean current efficacy was  $1.6 \cdot 10^{-5}$  with a standard deviation of  $0.9 \cdot 10^{-5}$ .

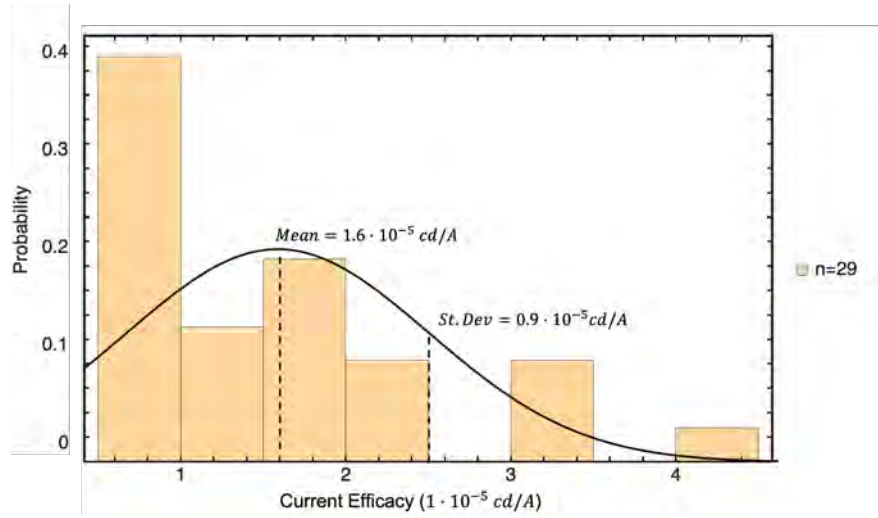


Figure 31: Distribution of patterned devices with on the x-axis the current efficacy and on the y-axis the probability of finding that efficacy.

#### 4.3 DISCUSSION

The absorption spectra, Tauch approximation and PL spectrum comparable with literature values with a bandgap of 2.3 eV and FWHM of 18 nm. The PL and EL spectra overlay are almost identical, which means that there is no significant influence from the HIL and EIL for the emission colour. The PL spectrum is measured at room temperature. This is, in principle, also the temperature where the devices are under during operation. The XRD measurement of the flat device was measured and as expected it showed small grains. In addition, the grainsize counts from the AFM confirms these small grains. SEM images of flat devices showed little degradation due to the electron beam at the perovskite surface. This can be seen due to the black spots on the grains. Furthermore, the grain size dimensions are based on dimension measurements in the FEI HELIOS 600. This is measured by eye, and grain size dimensions can differ. However, measuring was carried out as precise as possible. The AFM data, on the other hand, would be more accurate. The AFM software has the ability to watershed the grains and shows a distribution of grain sizes.

The parameters of choosing a suitable model are also based on getting the best model comparable with the AFM image dimensions. However, changing model parameters can lead to slightly different distributions of counts. The SEM and AFM images show more or less the same result in grain size. The roughness measurements, on the other hand, are exact with AFM measurements and analysis. On average, an RMS of 7.2 nm on a 10×10 μm scale is modest in the optimised flat device. Also, this measurement is carried out when the Bruker Dimension Icon was calibrated, which always leaves room for slight

differences based on calibration settings.

The JVL raw data was analysed in Mathematica and showed for optimised flat devices reproducible results. Turn-on voltages can always differ slightly from sample to sample and from pixel to pixel even. However, the overall performance of the PeLEDs was significantly more constant in the optimised devices than earlier runs with a relative error of  $\pm 35\%$  to more than 200% respectively. The flat device distribution is based on two runs with an identical recipe. Although this recipe was the same, adding these devices together led to a slightly larger standard deviation and a slightly larger relative error. The geometry of the setup during measurements was the same during all JVL measurements. Setup values were given by the company (Ossila). For the OLED Lifetime System, the calibration was done by the company when bought just before the project. Measurements in another calibrated system gave the same order of magnitude as the OLED Lifetime System (Paois by FLuxim). For the emission itself, the assumption is made that the PeLEDs were Lambertian emitters. The current efficacy from the flat devices compared to literature values lack from one to three orders of magnitude in current efficacy. This can have many reasons. The foremost reasons are stability due to interference with moisture and oxygen during the multi-steps fabrication process; glovebox conditions because there can always exist contamination with other chemicals; storage of spincoated PEDOT:PSS substrates in cleanroom because this process happens in a cleanroom in air and PEDOT:PSS attracts water easily. In the glovebox, before spincoating, the ITO/PEDOT:PSS substrates were again annealed at 100 degrees to evaporate the water particles out of the substrate for 10 minutes. However, this could have been too short to get rid of the water completely. Another reason for lower values of current efficacy can be because the ideal spincoat procedure was not found in this work and that optimisation processes went into a non-ideal direction for MAPbBr<sub>3</sub>. Although all literature showed other spincoat procedures and copying literature procedures lead to malfunctioned PeLEDs.

The simulated data showed an absorption increase of  $\approx 3\%$  with the used pattern as well. To show a positive effect from the pattern with a relative error of  $\pm 35\%$  about 500 pixels needed to be fabricated to drop the standard deviation by a factor of 10. This is out of the scope of this project due to time, and therefore it is hard to tell if it would be possible to show an effect at all based on these results. This relative error is calculated by dividing the standard deviation value by the mean value of the distribution and multiply it by 100. The stamp used in this work had slightly different dimensions as earlier mentioned. The height and diameter were larger than the simulated pattern. However, during plasma etching, these dimensions shrunk to almost the



actual diameter and height. So in order to make the actual stamp, the plasma etching has to be accounted for. After optimising the sol-gel procedure on top of the PEDOT:PSS and ITO, the pattern was very homogeneous. After plasma etching away the solgel between the solgel nanostructures, the PEDOT:PSS layer showed a polymer-like structure. This polymer-like structure is confirmed with earlier AFM measurements to check the surface morphology of the HIL (See appendix 35 for illustration of the polymer network structure).

XRD measurements showed no reason that the  $\text{MAPbBr}_3$  crystallised differently on patterned devices compared to flat devices (appendix 37). Therefore, complete devices were fabricated afterwards. These devices showed voids between the PEDOT:PSS layer and the  $\text{MAPbBr}_3$ . Three ways to counter this problem were tried: I) Before the spincoat procedure started, the  $\text{MAPbBr}_3$  was deposited on the substrate and 5 minutes of soaking time was given to lead the precursor solution to enter the patterns. II) The solvent material DMSO (Dimethylsulfoxide) is spincoated in advance the  $\text{MAPbBr}_3$  procedure. This increased the wettability between the pattern and the perovskite. III) Heating the precursor solution was the last option tried to get a more viscous solution that would better enter the pattern. Option I) and II) failed and showed no promising SEM images. Voids were still visible in these SEM images. In addition, these PeLEDs were tested and showed no response at the photodetector. Heating the precursor solution did show enhanced entering and crystallisation in between the solgel patterns. SEM images showed no more voids and as shown in 30, only nanostructures were visible in front of the cross section. However, due to more viscous precursor solution, spincoating resulted in thinner  $\text{MAPbBr}_3$  layers. Due to time limitations, this work stopped here with optimising patterned PeLEDs.

Whilst checking the operation of patterned PeLEDs during voltage sweeps. The PeLEDs lighted up, which was expected. However, the homogeneity issues as shown in 29a were still present. In order to show that the idea of nanophotonic manipulation at the emissive layer worked, all the pixels were analysed. The analysis of the performance was based on the full size of the stack. However, in most cases like 29a, not the whole pixel lighted up. This means that the performance of the patterned device is shown in 31 are underestimated. If the efficiency would be calculated for the part that lighted up, the current efficacy would be higher. The problem with the distribution of charge can probably be appointed to the voids remaining in the patterned devices. This is basically causing insulating voids where the charge does not conduct as efficiently as through the materials. Finally, the patterned devices showed a current efficacy that is one order of magnitude lower than in the flat devices. Current efficacy

is chosen as metric because most literature also uses current efficacy. This makes comparison more facile. Another metric that is used to measure light efficiency is Lumen per Watt and is also shown in equation 13. This metric is used at a further stage in commercialisation, such as displays of TVs and mobile phones, and is not applicable for this work.

The lower current efficacy can be appointed to the fact that in this project, significantly more time is spent on flat devices. Because in order to have a reference sample, the flat device needs to work first. Due to unseen problems at every step in optimising the fabrication, this took longer than initially expected. Therefore, the amount of time spent on optimisation of patterned devices lacks the flat. Therefore, not every step in optimising the patterned device was finished, leading to problems inside the device, such as voids.

In general, the stability of the  $\text{MAPbBr}_3$  was good. No actual degradation during fabrication was visible during fabrication. The stability of the PEDOT:PSS in ambient air is already discussed, but moisture problems can occur with PEDOT:PSS. This leads to contamination and different crystallisation during and after spincoating. The precursors for the histograms are made a day in advance of the spincoating procedures. After fabrication, the devices are stored in a nitrogen-filled glovebox, and JVL measurements are carried out a day later.





## CONCLUSION AND OUTLOOK

---

### 5.1 CONCLUSION

A proof of concept has been carried out in order to show nanophotonic manipulation inside full-stack perovskite LEDs. Flat PeLED devices have been optimised to become predictable and reproducible in performance. The MAPbBr<sub>3</sub> is characterised, and relatively small-grained perovskites are formed with grains 100 – 250 nm. The layer is smooth with an RMS of  $\approx 7$  nm. This crystallised layer has a bandgap value of 2.3 eV, which corresponds to literature values even as an FWHM of  $\approx 18$  nm. EL and PL measurements are compared and show almost identical spectra, which means that the influence of the other layers does not interfere with the performance. The crystallisation itself shows characteristic peaks at 15° and multiples without excess material peaks. Under operation, flat presented homogeneous green layers with an expected turn-on voltage around 3 V. The distribution of performance of the current efficacy was lower than literature values with a mean performance at  $15.8 \cdot 10^{-5}$  cd/A and a standard deviation of  $8 \cdot 10^{-5}$  cd/A.

Patterned devices show similar grain sizes as flat devices, and also, the patterned devices have a bandgap energy of 2.3 eV. Ellipsometry data determined the  $n$  and  $k$  values for the simulation. The simulated data showed an increased absorption of 3%. The pattern was simulated; however, due to time limitations, another pattern that had almost identical dimensions was used. The pattern is applied at an extra added layer of solgel in between the HIL and the perovskite. Plasma etching of the ITO/PEDOT:PSS/solgel substrate showed good properties for full-stack patterned devices in SEM imaging. AFM measurements from PEDOT:PSS layers support this data. After spincoating MAPbBr<sub>3</sub> on top of these substrates, XRD showed almost identical crystalization. However, voids occurred, and inhomogeneous distribution of charge was presented in the PeLEDs. The viscosity dropped by heating the precursor solution at fabrication temperatures, and better cohesion between the perovskite and the HIL is shown. In terms of efficiency, the patterned devices show a mean current efficacy of  $1.6 \cdot 10^{-5}$  cd/A with a standard deviation of  $0.9 \cdot 10^{-5}$  cd/A. Patterned devices are not yet more efficient than flat devices. This can be attributed to the fact that the patterned devices are not fully optimised yet. However, it succeeded as proof of concept that perovskite LEDs can be fabricated with a nanopattern without dam-

aging the perovskite itself.

Finally, the essence of this work is to contribute to energy efficiency. To get more efficient LEDs from novel materials and techniques that would increase light-outcoupling and thereby reduce the electricity consumption because of this enhanced outcoupling.

## 5.2 OUTLOOK

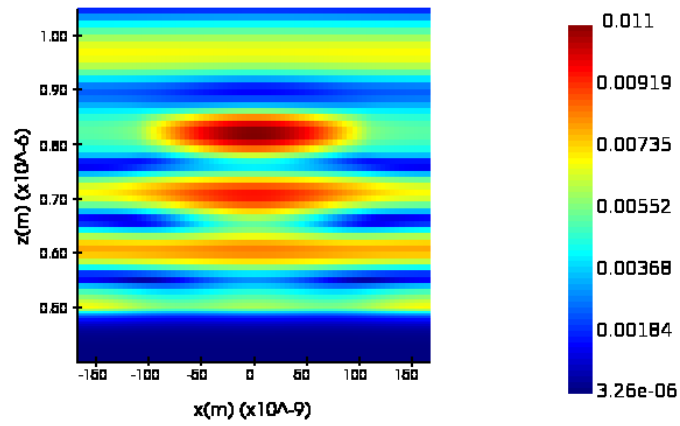
As a suggestion to do as future work in order to show a positive enhancement due to nanopatterning of the active layer: is to optimize the patterned devices for a longer period of time. To create a homogeneous layer with better cohesion that lights up under operation while keeping the dimensions of the full device the same. Future work could also include the use of other perovskites that would have even smaller grains to fit better between the structures, however more adjustments in the band alignment need to be made then. To increase the current efficacy, other perovskites could be used as well if one is interested in higher current efficacies.

In terms of patterning, for this work, it would be interesting to see if the simulated pattern could actually be used and how the perovskite crystals would fit in that pattern. To see what the effect of other patterns on the performance of PeLEDs would be.

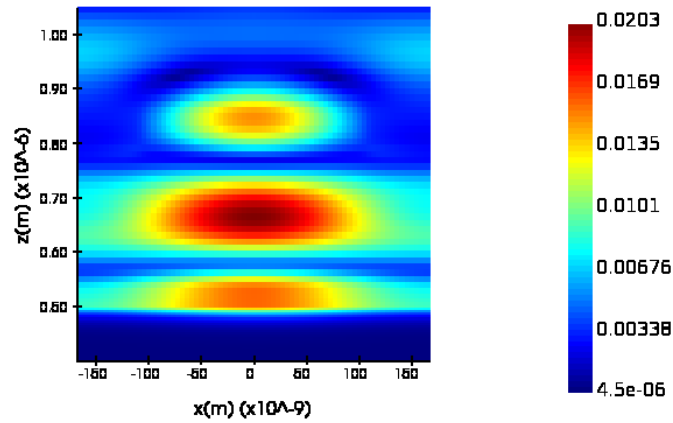
## APPENDIX

In this section extra data is given about measurements that did not fit in the thesis itself.

Figure 32 and 33 show increased magnetic (B) and electric (E) field intensities at 535 and 544 nm in the simulated nanostructures.

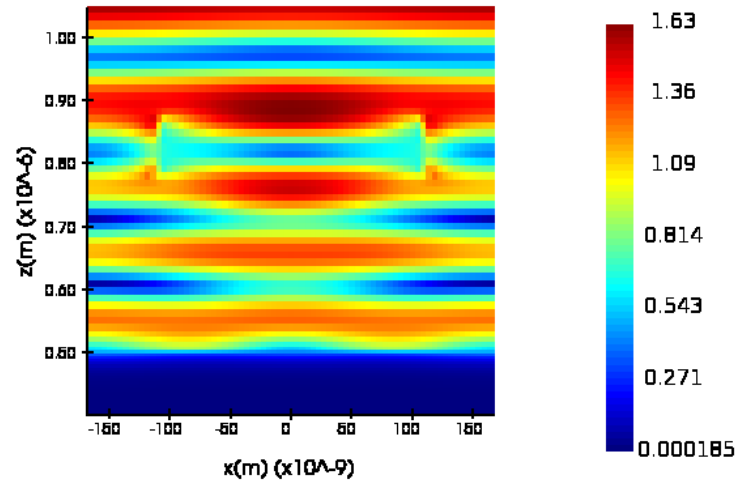


(a) H- field intensity at 535 nm

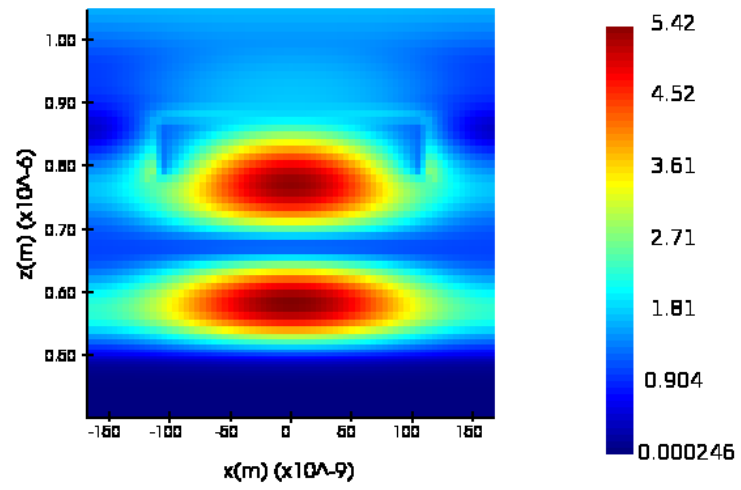


(b) H- field intensity at 544 nm

Figure 32: H-field enhancement



(a) E- field intensity at 535 nm



(b) E- field intensity at 544nm

Figure 33: E-field enhancement

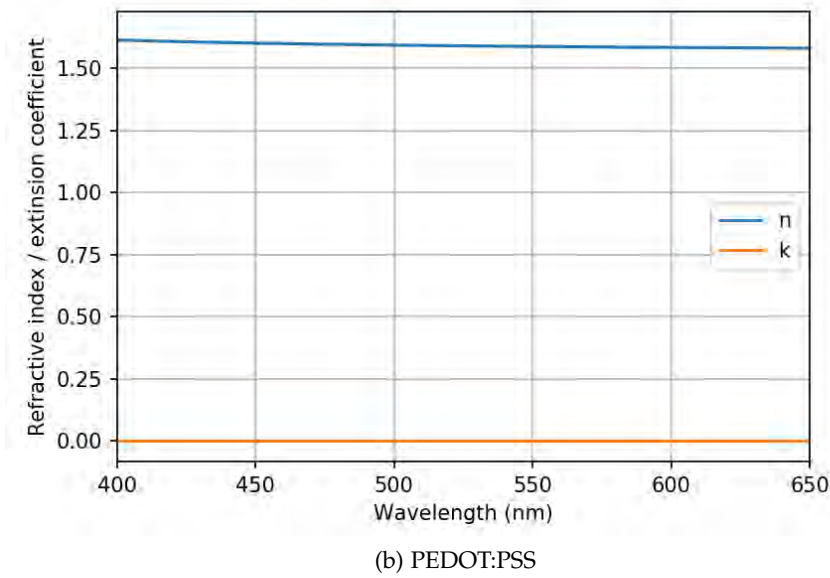
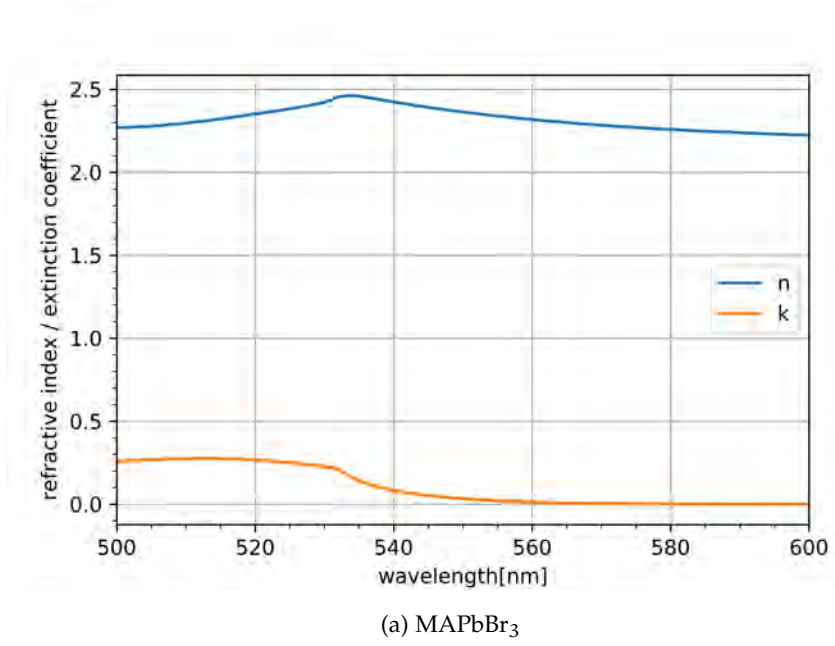


Figure 34: Fitted data from ellipsometry data from MAPbBr<sub>3</sub> and PEDOT:PSS where  $n$  is the refractive index and  $k$  the extinction coefficient

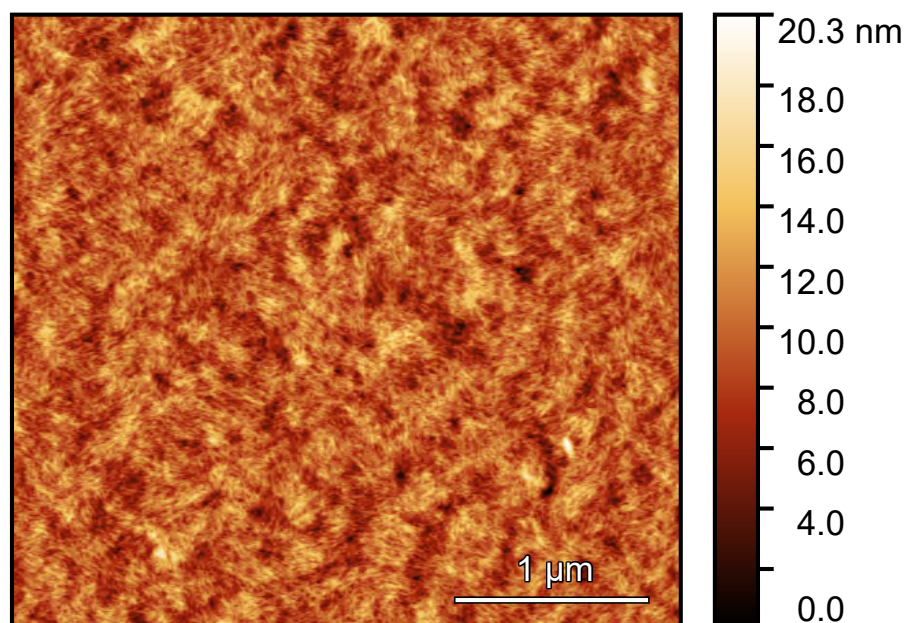


Figure 35: AFM PEDOT:PSS layer on top of ITO/glass substrate.

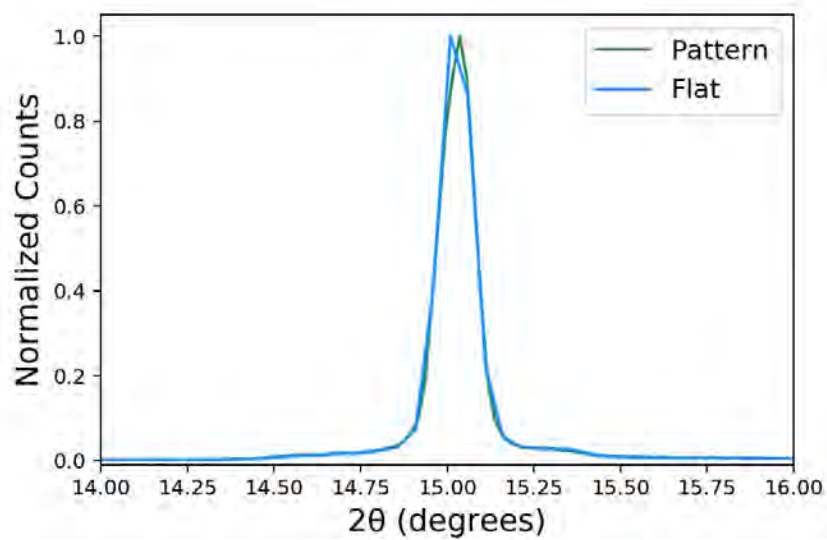


Figure 36: (001) Peak showed almost complete overlap in XRD measurements.

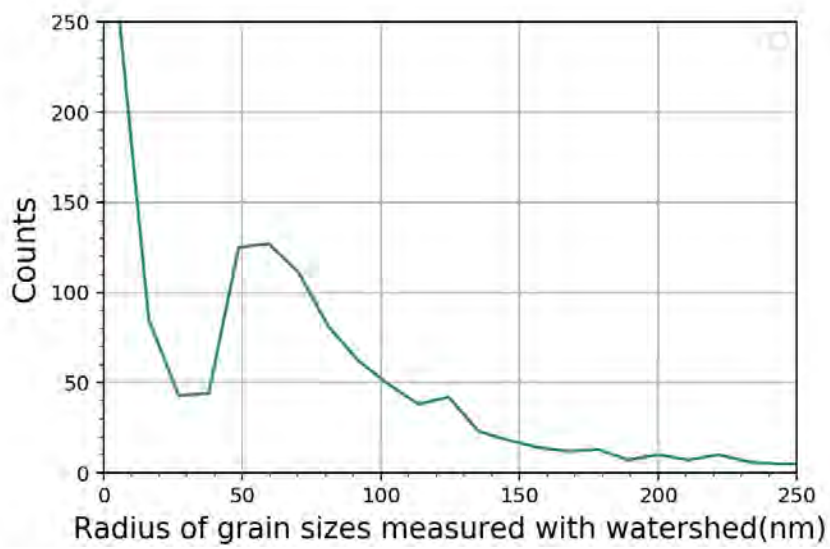


Figure 37: This figure shows the raw data from the watershed measurements. The y-axis show the counts and the x-axis the grain size radius





## BIBLIOGRAPHY

---

- [1] European Environment Agency. *Climate change is one of the biggest challenges of our times*. <https://www.eea.europa.eu/themes/climate>. Visited: August 10, 2021.
- [2] United Nations. *Climate Change 'Biggest Threat Modern Humans Have Ever Faced', World-Renowned Naturalist Tells Security Council, Calls for Greater Global Cooperation*. <https://www.un.org/press/en/2021/sc14445.doc.htm>. Visited: August 10, 2021.
- [3] G. Zissis. "Energy Consumption and Environmental and Economic Impact of Lighting: The Current Situation." In: *Handbook of Advanced Lighting Technology* (2016), pp. 1–13.
- [4] Zhu N. Zhang M. Wang L. Xing J. Zhang K. "Opportunities and challenges in perovskite LED commercialization." In: *Journal of Materials Chemistry C* 9(11) (2021), pp. 3795–3799.
- [5] Sheng S. Li. *Semiconductor Physical Electronics*. 2nd. New York, NY: Springer Science Business Media, 2006.
- [6] Grand View Research. *LED Modular Display Market Size, Share Trends Analysis Report By Type (Indoor Modular Screens, Outdoor Modular Screens), By Region, And Segment Forecasts, 2020 - 2027*. <https://www.grandviewresearch.com/industry-analysis/led-modular-display-market>. September 2020, Visited: August 10, 2021.
- [7] Anaya M. Abfalterer A. Stranks S. D. Ji K. "Halide Perovskite Light-Emitting Diode Technologies." In: *Advanced Optical Materials* (2021).
- [8] Sai Kim Vincent Lamboll Robin Shivanna Ravichandran Auras Florian Richter Johannes M. Yang et al. Zhao Baodan Bai. "High-efficiency perovskite–polymer bulk heterostructure light-emitting diodes." In: *Nature Photonics* 12(12) (2018), pp. 783–789.
- [9] He Tian Jingshu Guo Yingqiang Wei Hong Chen Yanfeng Miao Wei Zou Kang Pan Yarong He Hui Cao You Ke Mengmeng Xu Ying Wang Ming Yang Kai Du Zewu Fu Decheng Kong Daoxin Dai Yizheng Jin Gongqiang Li Hai Li Qiming Peng Jianpu Wang Wei Huang Yu Cao Nana Wang. "Perovskite light-emitting diodes based on spontaneously formed submicrometre-scale structures." In: *Nature* 562(7726) (2018), pp. 249–253.
- [10] Megens M. Ni Y. Van Sprang H. Polman A. Verschuuren M. "Large area nanoimprint by substrate conformal imprint lithography (SCIL)." In: *Advanced Optical Technologies* 6(3-4) (2017), pp. 243–264.

- [11] Basu C. Meinhardt-Wollweber M. Roth B. Singh D. "LEDs for Energy Efficient Greenhouse Lighting." In: *Renewable and Sustainable Energy Reviews* 49 (2015), pp. 139–147.
- [12] Jeong S. H.-Park M. H. Kim Y. H. Wolf C. Lee C. L. ... Lee T. W. Cho H. "Overcoming the electroluminescence efficiency limitations of perovskite light-emitting diodes." In: *Science* 350(6265) (2015), pp. 1222–1225.
- [13] D. B. Mitzi. "Introduction: perovskites." In: *Chemical reviews* 119(5) (2019), pp. 3033–3035.
- [14] K.; Kagan C. R. Mitzi D. B.; Chondroudis. "Organic-inorganic electronics." In: *IBM journal of research and development* 45(1) (2001), pp. 29–45.
- [15] Das S. Guggilla P. Brantley C. Sunda-Meya A. MChilvery A. "A perspective on the recent progress in solution-processed methods for highly efficient perovskite solar cells." In: *Science and Technology of advanced MaTerialS* 17(1) (2016), pp. 650–658.
- [16] Teshima K. Shirai Y. Miyasaka T. Kojima A. "Organometal halide perovskites as visible-light sensitizers for photovoltaic cells." In: *Journal of the American Chemical Society* 131(17) (2009), pp. 6050–6051.
- [17] Moghaddam R. S. Lai M. L. Docampo-P. Higler R. Deschler F. ... Friend R. H. Tan Z. K. "Bright light-emitting diodes based on organometal halide perovskite." In: *Nature nanotechnology* 9(9) (2014), pp. 687–692.
- [18] Ringler M. Klar T. A. Feldmann J. Munoz Javier A. Parak W. J. Dulkeith E. "Gold nanoparticles quench fluorescence by phase induced radiative rate suppression." In: *Nano letters* 5(4) (2005), pp. 585–589.
- [19] Jonas F. Freitag D. Pielartzik H. Reynolds J. R. Groenendaal L. "Poly (3, 4-ethylenedioxythiophene) and its derivatives: past, present, and future." In: *Advanced materials* 12(7) (2000), pp. 481–494.
- [20] Ossila. *TPBi*, <https://www.ossila.com/products/tpbi>. Visited: August 10, 2021.
- [21] Kirman J. Ma D. Sargent E. H. Quintero-Torres R. Quintero-Bermudez R. "Mechanisms of LiF Interlayer Enhancements of Perovskite Light-Emitting Diodes." In: *The journal of physical chemistry letters* 11(10) (2020), pp. 4213–4220.
- [22] Rand B. P. Holmes R. J. Credgington D. Bolink H. J. Friend R. H. ... Stranks S. D. Anaya M. "Best practices for measuring emerging light-emitting diode technologies." In: *Nature Photonics* 13(12) (2019), pp. 818–821.

- [23] Alex Ryer. *Light measurement handbook: Ultraviolet Light and visible light*. 1997.
- [24] Centronic. *Eye Response Detectors (series -E)*. <http://www.farnell.com/datasheets/1794403.pdf>. Visited: August 24, 2021.
- [25] Schubert E. Fred. *Light-Emitting Diodes*. 2nd. The Edinburgh Building, CB2 8RU, UK: Cambridge University Press, 2006.
- [26] Zhang Y. Wang S. Guo J. Yu W. W. Rogach A. L. Lu M. "Metal halide perovskite light-emitting devices: promising technology for next-generation displays." In: *Advanced Functional Materials* 29(30) (2019), p. 1902008.
- [27] Frydendahl C. Indukuri S. R. K. C. Mazurski N. Arora P. Levy U. Kessel A. "Soft Lithography for Manufacturing Scalable Perovskite Metasurfaces with Enhanced Emission and Absorption." In: *Advanced Optical Materials* 8(23) (2020), p. 2001627.
- [28] Furasova A. Tiguntseva E. Hemmetter A. Berestennikov A. Pushkarev A. ... Kivshar Y. Makarov S. "Halide-perovskite resonant nanophotonics." In: *Advanced Optical Materials* 7(1) (2019), p. 1800784.
- [29] Komissarenko FE et al Tiguntseva EY Zograf GP. "Light-emitting halide perovskite nanoantennas." In: *Nano Lett* 18 (2018), 1185–90.
- [30] Kolkowski R. Koenderink A. F. Staude I. Vaskin A. "Light-emitting metasurfaces." In: *Nanophotonics* 8(7) (2019), pp. 1151–1198.
- [31] Megens M. Ni Y. van Sprang H. Polman A. Verschuuren M. A. "Large area nanoimprint by substrate conformal imprint lithography (SCIL)." In: *Advanced Optical Technologies* 6(3-4) (2017), pp. 243–264.
- [32] University of Birmingham. *What does the Young's Modulus tell us about a material?* <https://www.birmingham.ac.uk/teachers/study-resources/stem/Physics/youngs-modulus.aspx#variable>. Visited: August 24, 2021.
- [33] Nan R. Jian Z. Li X. Shen H. "Defect step controlled growth of perovskite MAPbBr<sub>3</sub> single crystal." In: *Journal of Materials Science* 54(17) (2019), pp. 11596–11603.



## COLOPHON

This document was typeset using the typographical look-and-feel classicthesis developed by André Miede. The style was inspired by Robert Bringhurst's seminal book on typography "The Elements of Typographic Style". Changes have been made to the original document by David Langhorst August, 2021.

